

THE SPATIAL CLUSTERING OF ROSAT ALL-SKY SURVEY AGNS
III. EXPANDED SAMPLE AND COMPARISON WITH OPTICAL AGNSMIRKO KRUMPE^{1,2}, TAKAMITSU MIYAJI^{3,4}, ALISON L. COIL^{1,5}, AND HECTOR ACEVES³*Draft version October 27, 2011*

ABSTRACT

This is the third paper in a series that reports on our investigation of the clustering properties of AGNs identified in the *ROSAT* All-Sky Survey (RASS) and Sloan Digital Sky Survey (SDSS). In this paper, we extend the redshift range to $0.07 < z < 0.50$ and measure the clustering amplitudes of both X-ray and optically-selected SDSS broad-line AGNs with and without radio detections as well as for X-ray selected narrow-line RASS/SDSS AGNs. We measure the clustering amplitude through cross-correlation functions (CCFs) with SDSS galaxies and derive the bias by applying a halo occupation distribution (HOD) model directly to the CCFs. We find no statistically convincing difference in the clustering of X-ray and optically-selected broad-line AGNs, as well as with samples in which radio-detected AGNs are excluded. This is in contrast to low redshift optically-selected narrow-line AGNs, where radio-loud AGNs are found in more massive halos than optical AGNs without a radio-detection. The typical dark matter halo masses of our broad-line AGNs are $\log (M_{\text{DMH}}/[h^{-1} M_{\odot}]) \sim 12.4 - 13.4$, consistent with the halo mass range of typical non-AGN galaxies at low redshifts. We find no significant difference between the clustering of X-ray selected narrow-line AGNs and broad-line AGNs. We confirm the weak dependence of the clustering strength on AGN X-ray luminosity at a $\sim 2\sigma$ level. Finally, we summarize the current picture of AGN clustering to $z \sim 1.5$ based on three dimensional clustering measurements.

Subject headings: galaxies: active – X-rays: galaxies – cosmology: large-scale structure of Universe

1. INTRODUCTION

Galaxy clustering measurements of large area surveys, such as the 2dF Galaxy Redshift Survey (2dFGRS, Colless et al. 2001), Sloan Digital Sky Survey (SDSS, Abazajian et al. 2009), Deep Extragalactic Evolutionary Probe 2 Redshift Survey (DEEP2, Davis et al. 2003), AGN and Galaxy Evolution Survey (AGES, Kochanek et al. 2004), and VIMOS-VLT Deep Survey (VVDS, Le Fèvre et al. 2005) with many thousands of galaxies have quantified the clustering dependence on galaxy properties such as morphological type, luminosity, spectral type, and redshift to $z \sim 1$ (e.g., Norberg et al. 2002; Madgwick et al. 2003; Zehavi et al. 2005b; Meneux et al. 2006; Coil et al. 2008; Meneux et al. 2009). The general trend is that red, more massive, brighter, and/or elliptical galaxies cluster more strongly than blue, less massive, fainter, and/or spiral galaxies. Halo occupation distribution (HOD) modelling of these results has shown that there is an almost linear increase in the mean number of satellite (non-central) galaxies as a function of increasing dark matter halo (DMH) mass (e.g., Zheng et al. 2007; Zehavi et al. 2011).

Compared to projected angular clustering measure-

ments, three dimensional (3D) clustering measurements have greater statistical accuracy and minimize systematic errors associated with model assumptions in using Limber's de-projection (Limber 1954). However, 3D correlation functions require extremely large numbers of objects with secure redshift information.

Clustering measurements of the auto-correlation function (ACF) of active galactic nuclei (AGNs) reveal how AGNs are spatially distributed in the Universe. These measurements can constrain the AGN host galaxies, determine the typical DMH mass in which AGNs reside and the distribution of AGNs with DHM mass, test theoretical model predictions, and address which physical processes are triggering AGN activity (e.g., Porciani et al. 2004; Gilli et al. 2005, 2009; Yang et al. 2006; Coil et al. 2007; Coil et al. 2009; Ross et al. 2009; Krumpe et al. 2010a; Cappelluti et al. 2010; Miyaji et al. 2011; Allevato et al. 2011). However, a major challenge in AGN clustering measurements is to overcome the limitation caused by the low space density of AGNs.

Narrow emission line diagnostics (e.g., Veilleux & Osterbrock 1987; Kauffmann et al. 2003) have been used to identify narrow-line AGNs at low redshifts. Large sky area surveys with extensive spectroscopic follow-up programs have recently allowed narrow-line AGN clustering measurements for samples of up to 90,000 AGNs (Li et al. 2006). Studies such as Wake et al. (2004), Li et al. (2006), Magliocchetti et al. (2004), and Mandelbaum et al. (2009) explore the clustering strength of low redshift ($z < 0.3$) narrow-line AGNs samples with respect to various AGN properties (e.g., black hole mass, radio emission). Optically-selected narrow-line AGNs have a clustering strength

mkrumpe@ucsd.edu

¹ University of California, San Diego, Center for Astrophysics and Space Sciences, 9500 Gilman Drive, La Jolla, CA 92093-0424, USA² European Southern Observatory, ESO Headquarters, Karl-Schwarzschild-Straße 2, 85748 Garching bei München, Germany³ IAUNAM-E (Instituto de Astronomía de la Universidad Nacional Autónoma de México, Ensenada), PO Box 439027, San Diego, CA, 92143-9027, USA⁴ Visiting Scholar, University of California, San Diego, Center for Astrophysics and Space Sciences, 9500 Gilman Drive, La Jolla, CA 92093-0424, USA⁵ Alfred P. Sloan Fellow

similar to all galaxies (both blue and red). Narrow-line radio-loud AGNs cluster more strongly than AGN without radio-emission and identical samples of quiescent galaxies. Consequently, denser environment of galaxies increase the probability of hosting a narrow-line radio-loud AGN.

Broad-line AGNs are, in general, more luminous than narrow-line AGNs. Moreover, their energy production dominates over the host galaxy star light. Large area optical surveys have spectroscopically identified tens of thousands of broad-line AGNs (e.g., Schneider et al. 2010; Croom et al. 2001). The co-moving number density of broad-line AGNs is very low in the low redshift universe ($z < 0.5$). The situation improves at higher redshifts as the co-moving AGN number distribution peaks at $z \sim 2$. Furthermore, a given observed area corresponds at higher redshift to a larger observed co-moving volume. These two facts favor broad-line AGN clustering measurements at $z \gtrsim 0.5$ (e.g., Porciani et al. 2004; Croom et al. 2005; Ross et al. 2009).

X-ray surveys have also been used to select AGNs. These surveys cover much less sky area, e.g., ~ 0.1 – 1 deg², than optical surveys. Further, they sample lower AGN luminosities than optical surveys and contain a significant fraction of obscured AGNs. In order to probe the required large observed co-moving volume needed for clustering measurements using these relatively small sky areas, 3D clustering measurements of X-ray selected AGNs have mainly been conducted at $z \gtrsim 0.8$ (e.g., Gilli et al. 2005, 2009; Yang et al. 2006; Coil et al. 2007).

Optically-selected AGNs at redshifts of $z \sim 1.0$ – 1.5 appear to reside in somewhat lower host DMH masses ($M_{\text{DMH}} \sim 10^{12-13} h^{-1} M_{\odot}$, e.g., Porciani et al. 2004; Coil et al. 2007; Ross et al. 2009) than *XMM-Newton* and *Chandra* selected AGN samples ($M_{\text{DMH}} \sim 10^{13-13.5} h^{-1} M_{\odot}$, e.g., Yang et al. 2006; Gilli et al. 2005, 2009; Coil et al. 2009; Allevato et al. 2011). Possible explanations of the differences in the clustering signals include either the presence of a large fraction of X-ray absorbed narrow-line type II AGNs in the *XMM-Newton* and *Chandra* samples or the different luminosities of the AGN samples. At lower redshifts 3D broad-line X-ray AGN clustering measurements have been associated with large uncertainties, due to small sample sizes (e.g., Mullis et al. 2004).

To achieve smaller uncertainties in AGN clustering measurements, Coil et al. (2009) use the cross-correlation function (CCF) of AGNs with a tracer set of galaxies that contains a large number of objects. The AGN ACF is then inferred from the CCF, which has many more pairs at a given separation and hence significantly reduces the uncertainties in the spatial correlation function compared with the direct measurements of the AGN ACF.

In Krumpe et al. (2010a) (hereafter paper I) we use the cross-correlation technique to calculate the CCF between broad-line X-ray selected AGNs from the *ROSAT* All Sky Survey (RASS) and SDSS Luminous Red Galaxies (LRGs) in the redshift range $0.16 < z < 0.36$. The potential of RASS, which is currently the most sensitive X-ray all sky survey, can only be maximally exploited when it is combined with other large-area surveys such as SDSS. The unprecedented low uncertainties of the in-

ferred broad-line AGN ACF from the RASS/SDSS combination allows us to split our sample into subsamples according to their X-ray luminosities. From this work, for the first time, we report an X-ray luminosity dependence of broad-line AGN clustering in that higher luminosity AGNs cluster more strongly than their lower luminosity counterparts. We conclude that low luminosity broad-line RASS/SDSS AGNs cluster similarly to blue galaxies at the same redshift, while high luminosity RASS/SDSS AGNs cluster similarly to red galaxies.

In our second paper (Miyaji et al. 2011; hereafter paper II), we apply a halo occupation distribution (HOD) modeling technique to the AGN-LRG CCF in order to move beyond determining the typical DMH mass based on the clustering signal strength and instead constrain the full distribution of AGNs as a function of DMH mass. To do this, we develop a novel method of applying the HOD model directly to the CCF. The HOD modeling significantly improves the analysis of the CCF because it properly uses the Fourier transformed linear power spectrum in the “two halo term” as well as the non-linear growth of matter in the “one halo term” through the formation and growth of DMHs. This results in significant improvements over the standard method, which is used in paper I, of fitting both regimes with a phenomenological power law. One of the important results of this analysis is that at $0.16 < z < 0.36$ the mean number of satellite AGNs in a DMH does not proportionally increase with halo mass, as is found for satellite galaxies. The AGN fraction among satellite galaxies actually *decreases* with increasing DMH mass beyond $M_{\text{DMH}} \sim 10^{12} h^{-1} M_{\odot}$.

In this paper we extend the scope of our previous papers to both somewhat lower and higher redshifts to obtain broad-line AGN clustering results at $z < 0.5$, where very precise narrow-line AGN clustering measurements exist but broad-line AGN clustering is poorly constrained. This is crucial for studying the possible evolution and luminosity dependence of broad-line AGN clustering from low to high redshifts. The dominant process that triggers AGN activity could be a function of redshift and/or halo mass, which may be reflected in the clustering properties. We also study the clustering signal of both X-ray and optically-selected broad-line AGN samples, and test whether the exclusion of radio-detected broad-line AGNs changes our results. As the same statistical method and galaxy tracer sets are used to infer the clustering signal for X-ray and optically-selected broad-line AGNs, we can explore differences in the clustering among the different selection techniques with low systematic uncertainties. Furthermore, we derive bias parameters by applying the HOD modeling directly to all CCFs. In Paper II we show that using power law fit results even in the non-linear regime, as is commonly done in the literature, is appropriate to detect difference in the clustering properties between different samples. However, the derived bias parameters and DMH masses based on these fits should be interpreted with caution as the fit does not only consider the linear regime (two halo term), but also the non-linear regime (one halo term). Consequently, here we derive the bias for each AGN sample using HOD modeling of the CCF. Full detailed results of the HOD modeling of the CCFs presented in this paper will be given in a future paper (Miyaji et al. in preparation).

This paper is organized as follows. In Section 2 we

describe the properties of the different galaxy tracers sets used at different redshifts, while Section 3 gives the details of our different AGN samples. In Section 4 we briefly summarize the cross-correlation technique, how the AGN ACF is inferred from this, and present our results. We apply the HOD modeling in Section 5. Our results are discussed in Section 6 and we conclude in Section 7. Throughout the paper, all distances are measured in co-moving coordinates and given in units of h^{-1} Mpc, where $h = H_0/100 \text{ km s}^{-1} \text{ Mpc}^{-1}$, unless otherwise stated. We use a cosmology of $\Omega_m = 0.3$, $\Omega_\Lambda = 0.7$, and $\sigma_8(z=0) = 0.8$, which is consistent with the *WMAP* data release 7 (Larson et al. 2011; Table 3). The same cosmology is used in papers I & II. Luminosities and absolute magnitudes are calculated for $h = 0.7$. We use AB magnitudes throughout the paper. All uncertainties represent to a 1σ (68.3%) confidence interval unless otherwise stated.

2. GALAXY TRACER SETS

The crucial ingredient in the cross-correlation method is the tracer set, a sample with a large number of objects that traces the underlying dark matter density distribution. The properties of the tracer set determines the redshift range over which the method can be applied. The AGN samples of interest are necessarily limited to the same redshift range and geometry as the corresponding tracer set. As the RASS/SDSS selected AGNs (Anderson et al. 2007) are based on the SDSS data release 5 (DR5), we consequently limit the tracer sets to the same survey geometry when we compute the clustering measurements of the X-ray selected AGN. The SDSS geometry and completeness are expressed in terms of spherical polygons (Hamilton & Tegmark 2004). This file is not publicly-available for DR5, therefore, we use the latest version available prior to DR5: the DR4+ geometry file⁶. However, optically-selected SDSS AGNs (Schneider et al. 2010) make use of the full SDSS survey (DR7). Consequently, we consider tracer sets from the DR7 geometry⁷ whenever we compute CCFs of optically-selected SDSS AGNs.

In the redshift range of $0.07 < z < 0.16$ we use SDSS main galaxies for the tracer set, while SDSS luminous red galaxies (LRGs, Eisenstein et al. 2001) are used for the corresponding cross-correlation sample at $0.16 < z < 0.36$ (same as for paper I). Very luminous red galaxies are used as a tracer set at $0.36 < z < 0.50$. We will refer to the latter sample as the ‘extended LRG sample’. Above $z \sim 0.5$ the number of galaxies with spectroscopic redshifts in SDSS decreases dramatically and does not allow the selection of further tracer sets with a sufficient density of objects. In the following subsections we describe in detail the extraction of the various tracer sets and how we account for SDSS fiber collisions.

2.1. SDSS Main Galaxy Sample

The SDSS Main Galaxy sample (Strauss et al. 2002) is drawn from the NYU Value-Added Galaxy catalog⁸ (NYU VAGC, Blanton et al. 2005a; Padmanabhan et al. 2008), based on the SDSS DR7 (Abazajian et al. 2009).

The photometric data covers an area of 10417 deg^2 , while the spectroscopic data covers 7966 deg^2 . Absolute magnitudes, based on Petrosian fluxes, are K -corrected to $z = 0.1$ (Blanton et al. 2003; Blanton & Roweis 2007), which is close to the median redshift of our sample. We follow a scheme similar to Zehavi et al. (2005b), who use the NYU VAGC to measure the clustering of various luminosity and color-selected galaxy subsamples. Similarly, we limit our sample to $14.5 < r < 17.5$. The bright limit avoids incompleteness due to galaxy deblending, and the faint limit accounts for the slightly-varying r -band magnitude limit over the SDSS area (nominal value $r \sim 17.7$). The restriction of $r < 17.5$ ensures a uniform flux limit throughout the whole SDSS survey. In addition, we create a volume-limited galaxy sample by selecting objects with an absolute magnitude of $-22.1 < M_r^{0.1} < -21.1$. Finally we limit the redshift range to $0.07 < z < 0.16$.

Applying the above-mentioned selection criteria and considering only SDSS DR7 areas with a spectroscopic completeness ratio of >0.8 , we select 68273 galaxies with spectroscopic redshifts from the corresponding NYU VAGC. The DR7 area covered by restricting the spectroscopic completeness ratio to >0.8 is 7670 deg^2 . The properties of this DR7 SDSS main galaxy sample are summarized in Table 1.

As described above, the X-ray selected RASS/SDSS AGN samples are based on DR5. Therefore, we further reconfigure the DR7 tracer sets (in this case the SDSS main galaxy sample) to the DR4+ geometry to define a common survey geometry to use when measuring the clustering of X-ray selected AGNs. The restriction to the DR4+ survey area with a DR7 spectroscopic completeness ratio of >0.8 corresponds to an area of 5468 deg^2 . Table 1 lists the properties of the DR4+ SDSS Main Galaxy sample.

2.1.1. Accounting for the SDSS Fiber Collision

An operational constraint of the SDSS spectroscopic program is that two fibers cannot be placed closer than 55 arcsec on a single plate. Overlapping spectroscopic plates compensate partially for the effect. However, $\sim 7\%$ of the target galaxies cannot be spectroscopically observed because of fiber collisions. This observational bias is corrected by assigning to each galaxy that has not been observed the redshift of their nearest neighbor with a spectroscopic SDSS redshift (Blanton et al. 2005a).

Although one might be concerned that this simple method could overcorrect and result in too many close galaxy pairs at the same redshift, which would then distort clustering measurements, Zehavi et al. (2005b) demonstrate that this correction procedure works very well. They use Λ CDM N -body simulations and design three galaxy samples and measure the correlation function for three samples: i) from the full simulated galaxy distribution, ii) from simulated SDSS data including fiber collision losses and not correcting for it, and iii) from simulated SDSS data that corrects for the fiber collision by assigning the redshift of their nearest spectroscopic neighbor. They verify that the differences between i) and iii) are much smaller than the statistical uncertainties down to scales of $r_p \sim 0.1 h^{-1} \text{ Mpc}$, while ii) underestimates the correlation function at scales $r_p < 1 h^{-1}$

⁶ <http://sdss.physics.nyu.edu/lss/dr4plus>

⁷ <http://sdss.physics.nyu.edu/lss/dr72>

⁸ <http://sdss.physics.nyu.edu/vagc/>

Mpc. Therefore, we use the same fiber correction procedure for our main galaxy sample. The NYU VAGC⁹ provides this information through an SDSS fiber collision corrected galaxy sample.

2.1.2. Construction of the Random Main Galaxy Sample

The random sample is another crucial ingredient required for measuring the correlation function. The purpose is to create a randomly-distributed sample of objects that exactly matches all observational biases (window function, redshift distribution, etc.) of the observed sample. We follow the procedure of paper I (for details see paper I, Section 3.1) and generate a set of random *RA* and *Dec* values within DR7 areas with a spectroscopic completeness ratio of >0.8 , populate areas with higher completeness ratios more than areas with lower completeness ratios, smooth the observed redshift distribution by applying a least-square (Savitzky & Golay 1964) low-pass filter, and use this smoothed redshift profile to randomly assign redshifts to the objects in the sample.

The number of objects in a random catalog is chosen to have an adequate number of pairs in the CCF at the smallest scales measured here. For clustering measurements with the main galaxy sample the random catalog contains 100 times as many objects as the observed sample. The random catalog of the DR4+ SDSS main galaxy sample also contains 100 times more objects than the data and follows the same exact procedure described for the DR7 geometry, except that we restrict that area to the DR4+ geometry.

2.2. SDSS Luminous Red Galaxy Sample

The selection of the SDSS LRG sample is described in detail in Section 2.1 of paper I. Here we briefly summarize the sample selection. We extract LRGs from the web-based SDSS Catalog Archive Server Jobs System¹⁰ using the flag ‘galaxy_red’, which is based on the selection criteria defined in Eisenstein et al. (2001). We verify that the extracted objects meet all LRG selection criteria and create a volume-limited sample with $0.16 < z < 0.36$ and $-23.2 < M_g^{0.3} < -21.2$, where $M_g^{0.3}$ is based on the extinction-corrected r_{petro}^* magnitude to construct the k -corrected and passively evolved rest-frame g_{petro}^* magnitudes at $z = 0.3$. We consider only LRGs that fall into the SDSS area with a DR7 spectroscopic completeness ratio of >0.8 and have a redshift confidence level of >0.95 .

The correction for the SDSS fiber collision in the SDSS LRG sample is slightly different from that for the SDSS main galaxy sample. LRGs exhibit very well-defined spectra dominated by an old stellar population that evolves very slowly. The reduced scatter in the spectral energy distribution (SED) of LRGs results in much lower photometric redshift uncertainties than the estimates for main galaxies, which can have ongoing star formation and therefore have a wider distribution of SEDs. We make use of the precise LRG photometric redshifts to correct for the SDSS fiber collision in the following manner. We select from the SDSS archive all LRGs that pass

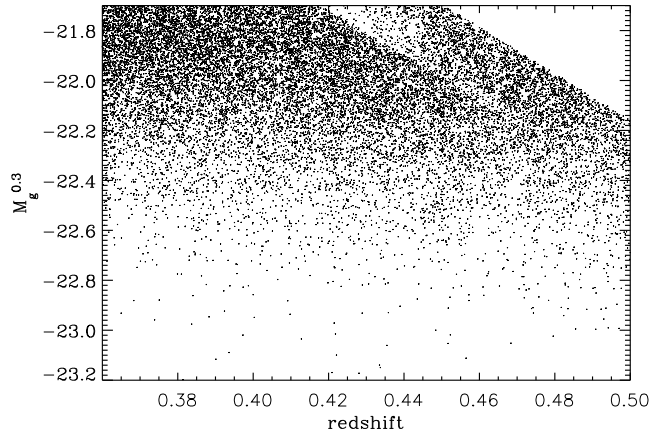


FIG. 1.— Absolute magnitude versus redshift for the extended SDSS luminous red galaxy sample ($0.36 < z < 0.50$). The absolute magnitude is based on the extinction-corrected r_{petro}^* magnitude, passively evolved to $z = 0.3$. The different selection criteria for low and high redshift LRGs are visible in the upper right corner (cut I and cut II, see Eisenstein et al. 2001).

the pure photometric-based LRG selection criteria. We identify photometric LRGs that are closer than 55 arcsec to a spectroscopic observed LRG in our redshift and absolute magnitude range. We then assign a redshift using the following steps: we accept the spectroscopic redshift of the LRG even if its redshift confidence level is ≤ 0.95 . If there is no spectroscopic redshift available for the object, we give the photometric LRG the same redshift as the spectroscopic neighbor LRG (within a 55 arcsec radius) if

$$|z_{\text{spec},j} - z_{\text{photo},i}| \leq \delta z_{\text{photo},i,1\sigma}. \quad (1)$$

If Equation 1 is not fulfilled, we assume that the photometric redshift of the LRG is the correct redshift. A redshift is assigned only if the object meets the selection criteria to construct a volume-limited sample: $0.16 < z < 0.36$ and $-23.2 < M_g^{0.3} < -21.2$. Approximately 2% of the all LRGs in our sample are assigned redshifts. The properties of the sample are shown in Table 1.

The construction of the random catalogs is identical to the procedure described in Section 2.1.2 (for details see paper I, Section 3.1), except that the LRG random catalogs contain 200 times as many objects as the real DR7 and DR4+ LRG samples. This is a compromise between the required computation time to calculate the correlation functions and having sufficient counts on the smallest scales to avoid introducing noise. More objects are required at higher redshift for a given sky area to account for the fact that with increasing redshift the same angular distance on the sky corresponds to larger physical co-moving separations.

2.3. Extended SDSS Luminous Red Galaxy Sample

In order to extend our clustering measurements to higher redshifts, we create an “extended SDSS LRG sample” over the redshift range of $0.36 < z < 0.50$. The extraction of the sample and the correction for the SDSS fiber collision problem is identical to the SDSS LRG sample (see Section 2.2).

Identifying spectroscopic neighbors would also be volume-limited. However, that would require an absolute magnitude cut

⁹ <http://sdss.physics.nyu.edu/vagc-dr7/vagc2/kcorrect/kcorrect.html>
¹⁰ <http://casjobs.sdss.org/CasJobs/>

TABLE 1
PROPERTIES OF THE SDSS GALAXY TRACER SETS AND THE AGN SAMPLES.

Sample Name	SDSS Geometry	z -range	$M, \log L_X$ range (mag, erg s $^{-1}$)	Sample Size	$\langle n \rangle$ (h^3 Mpc $^{-3}$)	$\langle z \rangle$	$\langle M, \log L_X \rangle$ (mag, erg s $^{-1}$)
SDSS Tracer Sets							
Main galaxy sample	DR7	$0.07 < z < 0.16$	$-22.1 < M_r^{0.1} < -21.1$	68273	9.8×10^{-4}	0.13	-21.41
	DR4+	$0.07 < z < 0.16$	$-22.1 < M_r^{0.1} < -21.1$	48994	9.8×10^{-4}	0.13	-21.41
LRG sample	DR7	$0.16 < z < 0.36$	$-23.2 < M_g^{0.3} < -21.2$	65802	9.8×10^{-5}	0.28	-21.71
	DR4+	$0.16 < z < 0.36$	$-23.2 < M_g^{0.3} < -21.2$	45899	9.6×10^{-5}	0.28	-21.71
Extended LRG sample	DR7	$0.36 < z < 0.50$	$-23.2 < M_g^{0.3} < -21.7$	28781	3.9×10^{-5}	0.42	-22.04
	DR4+	$0.36 < z < 0.50$	$-23.2 < M_g^{0.3} < -21.7$	19831	3.8×10^{-5}	0.42	-22.04
X-ray Selected AGNs – RASS/SDSS AGNs							
total RASS-AGN	DR4+	$0.07 < z < 0.16$	$43.05 \lesssim \log L_X \lesssim 44.12$	629	5.2×10^{-5}	0.12	43.59
total RASS-AGN (rq)	DR4+	$0.07 < z < 0.16$	$43.04 \lesssim \log L_X \lesssim 44.04$	504	4.5×10^{-5}	0.12	43.55
low L_X RASS-AGN	DR4+	$0.07 < z < 0.16$	$42.92 \lesssim \log L_X \lesssim 43.54$	293	4.5×10^{-5}	0.11	43.25
high L_X RASS-AGN	DR4+	$0.07 < z < 0.16$	$43.54 \lesssim \log L_X \lesssim 44.27$	336	7.0×10^{-6}	0.13	43.89
low L_X RASS-AGN (rq)	DR4+	$0.07 < z < 0.16$	$42.93 \lesssim \log L_X \lesssim 43.54$	253	4.0×10^{-5}	0.11	43.26
high L_X RASS-AGN (rq)	DR4+	$0.07 < z < 0.16$	$43.54 \lesssim \log L_X \lesssim 44.16$	251	5.2×10^{-6}	0.13	43.85
narrow line RASS-AGN	DR4+	$0.07 < z < 0.16$	$42.81 \lesssim \log L_X \lesssim 43.81$	194	6.5×10^{-4}	0.11	43.32
total RASS-AGN	DR4+	$0.16 < z < 0.36$	$43.69 \lesssim \log L_X \lesssim 44.68$	1552	6.0×10^{-5}	0.25	44.17
total RASS-AGN (rq)	DR4+	$0.16 < z < 0.36$	$43.69 \lesssim \log L_X \lesssim 44.63$	1337	4.9×10^{-5}	0.25	44.15
low L_X RASS-AGN	DR4+	$0.16 < z < 0.36$	$43.62 \lesssim \log L_X \lesssim 44.29$	990	5.8×10^{-5}	0.24	43.94
high L_X RASS-AGN	DR4+	$0.16 < z < 0.36$	$44.29 \lesssim \log L_X \lesssim 44.87$	562	1.2×10^{-6}	0.28	44.58
low L_X RASS-AGN (rq)	DR4+	$0.16 < z < 0.36$	$43.64 \lesssim \log L_X \lesssim 44.29$	883	4.8×10^{-5}	0.24	43.95
high L_X RASS-AGN (rq)	DR4+	$0.16 < z < 0.36$	$44.29 \lesssim \log L_X \lesssim 44.82$	454	1.0×10^{-6}	0.28	44.55
narrow line RASS-AGN	DR4+	$0.16 < z < 0.36$	$43.50 \lesssim \log L_X \lesssim 44.40$	187	7.1×10^{-6}	0.24	43.92
total RASS-AGN	DR4+	$0.36 < z < 0.50$	$44.25 \lesssim \log L_X \lesssim 45.04$	876	8.5×10^{-5}	0.43	44.64
total RASS-AGN (rq)	DR4+	$0.36 < z < 0.50$	$44.24 \lesssim \log L_X \lesssim 44.99$	722	8.3×10^{-5}	0.43	44.61
Optically-Selected AGNs – SDSS AGNs							
total SDSS-AGN	DR7	$0.07 < z < 0.16$	$-23.26 \lesssim M_i \lesssim -22.06$	177	–	0.13	-22.52
total SDSS-AGN (rq)	DR7	$0.07 < z < 0.16$	$-23.01 \lesssim M_i \lesssim -22.06$	96	–	0.13	-22.45
total SDSS-AGN	DR7	$0.16 < z < 0.36$	$-23.27 \lesssim M_i \lesssim -22.07$	3500	–	0.28	-22.55
total SDSS-AGN (rq)	DR7	$0.16 < z < 0.36$	$-23.17 \lesssim M_i \lesssim -22.06$	2879	–	0.29	-22.51
total SDSS-AGN (noX)	DR7	$0.16 < z < 0.36$	$-23.09 \lesssim M_i \lesssim -22.06$	2367	–	0.29	-22.47
total SDSS-AGN (rq+noX)	DR7	$0.16 < z < 0.36$	$-22.98 \lesssim M_i \lesssim -22.05$	1958	–	0.29	-22.44
total SDSS-AGN (onlyX)	DR7	$0.16 < z < 0.36$	$-23.52 \lesssim M_i \lesssim -22.11$	1133	–	0.27	-22.72
low M_i SDSS-AGN	DR7	$0.16 < z < 0.36$	$-22.4 \lesssim M_i \lesssim -22.03$	1757	–	0.28	-22.18
high M_i SDSS-AGN	DR7	$0.16 < z < 0.36$	$-23.60 \lesssim M_i \lesssim -22.4$	1743	–	0.29	-22.93
low M_i SDSS-AGN (rq)	DR7	$0.16 < z < 0.36$	$-22.4 \lesssim M_i \lesssim -22.03$	1520	–	0.28	-22.18
high M_i SDSS-AGN (rq)	DR7	$0.16 < z < 0.36$	$-23.52 \lesssim M_i \lesssim -22.4$	1359	–	0.29	-22.88
total SDSS-AGN	DR7	$0.36 < z < 0.50$	$-23.89 \lesssim M_i \lesssim -22.36$	4404	–	0.43	-23.04
total SDSS-AGN (rq)	DR7	$0.36 < z < 0.50$	$-23.79 \lesssim M_i \lesssim -22.36$	3773	–	0.43	-23.01
total SDSS-AGN (noX)	DR7	$0.36 < z < 0.50$	$-23.72 \lesssim M_i \lesssim -22.35$	3421	–	0.43	-22.98
total SDSS-AGN (rq+noX)	DR7	$0.36 < z < 0.50$	$-23.65 \lesssim M_i \lesssim -22.35$	2960	–	0.43	-22.96
low M_i SDSS-AGN	DR7	$0.36 < z < 0.50$	$-22.9 \lesssim M_i \lesssim -22.22$	2059	–	0.42	-22.55
high M_i SDSS-AGN	DR7	$0.36 < z < 0.50$	$-24.24 \lesssim M_i \lesssim -22.9$	2345	–	0.44	-23.48
low M_i SDSS-AGN (rq)	DR7	$0.36 < z < 0.50$	$-22.9 \lesssim M_i \lesssim -22.24$	1804	–	0.42	-22.56
high M_i SDSS-AGN (rq)	DR7	$0.36 < z < 0.50$	$-24.13 \lesssim M_i \lesssim -22.9$	1969	–	0.44	-23.43

NOTE. — The notation $\langle \rangle$ characterizes the average (mean) value of the given quantity. The columns ‘ M, L_X range’ and ‘ $\langle M, L_X \rangle$ ’ specify absolute optical magnitudes for optical samples and galactic-absorption corrected 0.1–2.4 keV luminosities for X-ray selected samples. The absolute magnitudes are given for the SDSS filter band stated in the lower index and K -corrected to the redshift given in the upper index. The symbol “ \lesssim ” is used to characterize the “soft” luminosity boundary of the samples; it indicates the 10th (for the lower bound) or the 90th (for the upper bound) percentile. Note that unlike the main galaxy sample and the LRG sample, the extended LRG sample is not volume-limited. The listed co-moving number densities for the extended LRG samples are the number densities for the redshift range $0.36 < z < 0.42$ and $-23.2 < M_g^{0.3} < -21.7$, where the sample is volume-limited. The number densities of the X-ray selected AGN samples are calculated by computing the co-moving volume available to each object. For optically-selected AGNs, the selection function is complex enough that we do not derive number densities. Abbreviations: rq – radio-quiet AGNs only (see our definition of radio-quiet in Sections 3.1.1 and 3.2.1); noX – optically-selected SDSS AGNs that are not detected by RASS; onlyX – only optically-selected SDSS-AGNs that are also RASS detections.

of $M_g^{0.3} = -22.2$ mag, which results in only 6292 objects. As such a relatively low number of objects would yield a measured ACF with very large uncertainties, we use a non-volume-limited sample with $-23.2 < M_g^{0.3} < -21.7$. This is a compromise between making the sample volume-limited and retaining accuracy when computing the ACF and CCFs (see Table 1). We plot the absolute magnitude versus redshift for the 28781 objects (DR7) in the extended LRG sample in Fig. 1.

The co-moving number density for this sample given in Table 1 is computed over the redshift range $0.36 < z < 0.42$ and magnitude range $-23.2 < M_g^{0.3} < -21.7$, where the sample is volume-limited. Furthermore, it assumes that there is no number density evolution at higher redshifts ($0.36 < z < 0.42$) and in the range $-23.2 < M_g^{0.3} < -21.7$. In principle, we can derive the co-moving number density by integrating the LRG luminosity function. However, the different selection functions for low and high redshift LRGs (cut I and II, Eisenstein et al. 2001) are difficult to model and could result in large uncertainties. Therefore, we decide to limit the estimate to the volume-limited redshift range.

The random catalogs contain 1000 times as many objects as the data sample. The procedure follows the description in Section 2.1.2.

3. AGN SAMPLES

In this paper we derive the AGN ACF for X-ray and optically-selected SDSS AGN samples. The selection of the different AGN samples is described below.

3.1. RASS/SDSS AGN Samples

The *ROSAT* All-Sky Survey (RASS, Voges et al. 1999) is currently the most sensitive all-sky X-ray survey. Although relatively shallow, this data set has a huge potential for science, especially when combined with other large-area spectroscopic surveys such as SDSS. Anderson et al. (2003, 2007) positionally cross-correlated RASS sources with SDSS spectroscopic objects and classified RASS and SDSS-detected AGNs based on SDSS DR5. They find 6224 AGNs with broad permitted emission lines in excess of 1000 km s^{-1} FWHM and 515 narrow permitted emission line AGNs matching RASS sources within 1 arcmin. More details on the sample selection are given in paper I Section 2.2 and Anderson et al. (2003, 2007). The RASS/SDSS AGN sample is biased toward unabsorbed AGNs due to *ROSAT*'s soft energy band (0.1–2.4 keV). AGNs with broad emission lines and UV excess are, in general, known to show little to no X-ray absorption and therefore account for the vast majority of the RASS/SDSS AGNs.

The latest available version of the RASS/SDSS AGN sample is based on DR5 (Anderson et al. 2007). Therefore, we reconfigure the sample to publically-available DR4+ geometry. We select broad emission line AGNs in different redshift ranges according to the redshift ranges of the available galaxy tracer sets (see Fig. 2 and Table 1).

To study the X-ray luminosity dependence of the clustering, we further subdivide the AGNs in the redshift ranges of $0.07 < z < 0.16$ and $0.16 < z < 0.36$ into relatively lower and higher X-ray luminosity sam-

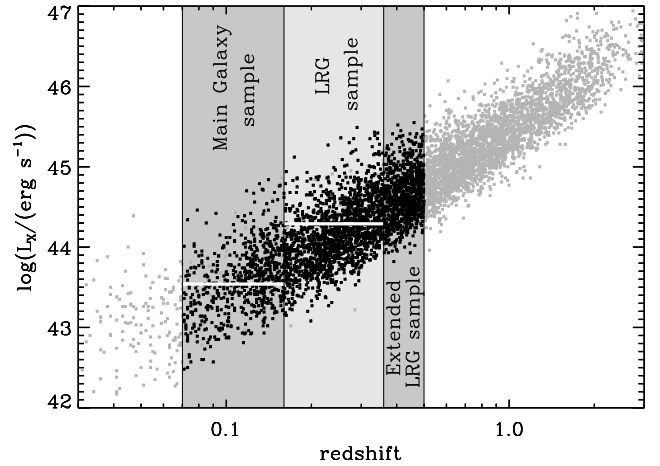


FIG. 2.— 0.1–2.4 keV observed X-ray luminosity versus redshift for the broad emission line AGN sample in SDSS DR5 determined by Anderson et al. (2007). Black symbols show objects used here in the redshift range of $0.07 < z < 0.50$. The shaded areas show the different AGN subsamples, labeled with the corresponding tracer set for the cross-correlation measurement. The horizontal white lines show the dividing line between the lower X-ray luminosity and higher X-ray luminosity RASS/SDSS AGN subsamples for $0.07 < z < 0.16$ $\log(L_{0.1-2.4 \text{ keV}} / [\text{erg s}^{-1}]) = 43.54$ and $0.16 < z < 0.36$ $\log(L_{0.1-2.4 \text{ keV}} / [\text{erg s}^{-1}]) = 44.29$.

ples. The RASS/SDSS AGNs in the redshift range of $0.36 < z < 0.50$ are not subdivided into a lower and higher X-ray luminosity sample, as the corresponding tracer set (extended LRGs) has a much lower number of objects than the other tracer sets. Consequently, there are too few pairs in the CCF and prohibitively large uncertainties to usefully compare the RASS/SDSS AGN ACF of lower and higher X-ray luminosity samples.

We use the 0.1–2.4 keV observed luminosity reported by Anderson et al. (2003, 2007), which assumes a photon index of $\Gamma = 2.5$ and is corrected for Galactic absorption. Our 0.1–2.4 keV luminosity cuts are $\log(L_X / [\text{erg s}^{-1}]) = 43.54$ for $0.07 < z < 0.16$ and $\log(L_X / [\text{erg s}^{-1}]) = 44.29$ for $0.16 < z < 0.36$ (see Fig. 2). Using $\Gamma = 2.5$, the luminosity cuts correspond to 0.5 – 10 keV luminosities of $(L_X / [10^{43} \text{ erg s}^{-1}]) = 1.5$ and 8.5 , respectively.

A significant overlap between broad-line RASS/SDSS AGNs and the SDSS main galaxy sample tracer set exists only in the lowest redshift range ($0.07 < z < 0.16$). For the low luminosity broad-line AGNs in that redshift range, the AGN light does not dominate the optical spectrum. Hence, 186 objects of the total RASS/SDSS AGN sample of 629 objects are also classified as SDSS main galaxies (52 within the low L_X AGN sample, 134 within the high L_X AGN sample). In the higher redshift samples, no match between RASS/SDSS AGN and the LRG tracer sets is found as the selection methods for LRGs and RASS/SDSS AGN are very different and high luminosity AGNs dominate the optical spectrum. To quantify the effect of the overlap between both samples, we create a SDSS main galaxy sample that does not include objects that have also been classified as RASS/SDSS AGNs. Compared with the original CCF, the CCF of this new sample shows differences of less than 1% in the pair counts on scales larger than $1.4 h^{-1} \text{ Mpc}$. This is well below the statistical uncertainty of the CCF itself, therefore, the overlap between the AGN sample and the tracer set will not significantly affect our clustering mea-

surements in the lowest redshift range.

We calculate the co-moving number densities given in Table 1 as described in detail in paper I. For a given $R.A.$ and Dec we compute the limiting observable RASS count rate and infer the absorption-corrected flux limit versus survey area for RASS/SDSS AGNs. We then compute the co-moving volume available to each object (V_a) for being included in the sample (Avni & Bahcall 1980). The co-moving number density follows by computing the sum of the available volume over each object $n_{AGN} = \sum_i 1/V_{a,i}$.

3.1.1. Radio-quiet RASS/SDSS AGN Samples

Radio-loud AGNs are known to be more clustered than radio-quiet AGNs and reside in very massive DMHs (e.g., Magliocchetti et al. 2004; Hickox et al. 2009; Mandelbaum et al. 2009). Radio-loud AGNs are also more luminous in the X-rays than radio-quiet AGNs (Wilkes et al. 1994; Krumpke et al. 2010b).

In paper I we find an X-ray luminosity dependence in the AGN clustering amplitude. One possible explanation is that the high L_X sample contains more radio-loud AGNs than the low L_X sample, and therefore the relative overabundance of radio-loud AGNs in the high L_X sample is causing the increase of the clustering amplitude. To test this hypothesis, we construct radio-quiet RASS/SDSS AGN samples. Anderson et al. (2003, 2007) list in their table of broad-line RASS/SDSS AGN if an object is also detected as a radio source. The radio information is taken from the Faint Images of the Radio Sky at Twenty centimeters (FIRST; Becker, White, & Helfand 1995; White et al. 1997) using the NRAO Very Large Array. We therefore create new AGN subsamples by restricting all samples to the area covered by FIRST and excluding all FIRST detected sources, and refer to these subsamples as radio-quiet X-ray selected AGN samples. FIRST and SDSS cover almost the same area (FIRST has $\sim 7\%$ less area than SDSS DR4+ and $\sim 5\%$ less area than SDSS DR7). We also limit the tracer sets to the FIRST geometry when computing CCFs of radio-quiet AGN samples and the corresponding tracer set ACFs.

In Tables 1, 2, and 3 we label these subsamples with the entry ‘(rq)’. Note that our approach is conservative, in that we do not apply the usual radio-to-optical flux density criteria of $R > 10$ (Kellermann et al. 1989). Instead we remove all radio-detected AGNs, which removes more objects than just those that are technically defined as radio-loud. Our definition of radio-quiet is that the AGNs are not detected by FIRST. However, for our goal of removing all radio-loud AGNs from the samples, the chosen procedure is adequate and the loss in a few additional AGNs will not significantly affect the clustering measurements and their uncertainties.

In the redshift range of $0.07 < z < 0.16$, 127 out of 504 objects are classified as radio-quiet RASS/SDSS AGNs and SDSS main galaxies. Since we find no significant difference in the CCF of samples that include or exclude these objects, we use the full sample. No overlap is found between radio-quiet RASS/SDSS AGNs and tracer set objects at higher redshifts.

In Fig. 3 we show the distribution of the RASS/SDSS AGNs which are flagged as radio sources by

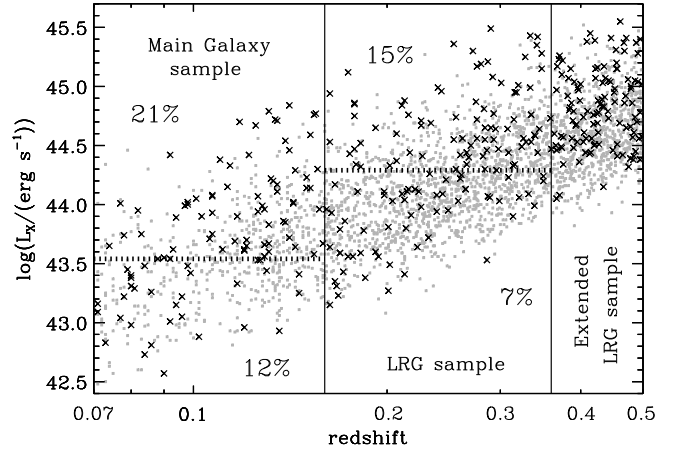


FIG. 3.— Location of FIRST radio-detected RASS/SDSS AGNs (crosses) in the 0.1-2.4 keV observed X-ray luminosity versus redshift plane for the studied DR4+ X-ray samples. Gray dots show RASS/SDSS AGNs without a FIRST radio detection, which we refer to as ‘radio-quiet’ RASS/SDSS AGN. We show only those objects that fall within the region covered by FIRST and SDSS. The solid vertical lines indicate the redshift ranges of the different samples, while the dotted horizontal lines show the luminosity cuts used to create the lower and higher X-ray luminosity samples (see Fig. 2 for details). The percentage values give the fraction of radio-detected RASS/SDSS AGNs in the corresponding lower and higher L_X samples.

Anderson et al. (2003, 2007), which we remove to create the ‘radio-quiet’ samples. Considering only objects that fall in regions covered by SDSS and FIRST, 17% of all RASS/SDSS AGN have radio detections in the $0.07 < z < 0.16$ range, 10% at $0.16 < z < 0.36$, and 14% at $0.36 < z < 0.50$. We also report the radio-detected AGN fraction in the corresponding lower and higher L_X samples as the percentage values listed in Fig. 3.

3.1.2. Narrow-line RASS/SDSS AGN Samples

In order to test narrow-line versus broad-line AGN clustering, we construct X-ray selected narrow-line AGN samples. In addition to the predominant broad-line AGNs, Anderson et al. (2007) classified $\sim 7\%$ of all RASS/SDSS AGNs as X-ray emitting AGNs having narrower permitted emission lines. These 515 objects consist of X-ray emitting AGN subclasses such as narrow-line Seyfert 1’s (NLS1s) (10%), Seyfert 1.5 (29%), Seyfert 1.8 (18%), Seyfert 1.9 galaxies (22%), and Seyfert 2 candidates (21%). In total, 22% of these objects also have a FIRST radio detection. NLS1s, Seyfert 1.5, 1.8, and 1.9 AGNs show a mix of narrow and broad permitted typical AGN line components, while Seyfert 2 candidates have only narrow permitted emission lines. The latter are called candidates because it is well known that a fair fraction of them turn out to be reclassified as NLS1, Seyfert 1.8, or Seyfert 1.9 when re-observed with significantly improved spectroscopy (e.g., Halpern et al. 1999). Seyfert 1.5 and 1.8 galaxies have optical spectra with a broad line $H\beta$ component (exceeding FWHM values of 2500 km s^{-1}) at a very low flux level. For more details about the different narrow-line AGN subclasses in this sample see Anderson et al. (2003, 2007). Figure 4 shows that the narrow-line RASS/SDSS AGNs are mainly identified only at lower redshifts, to $z \sim 0.35$. Therefore, their classification as narrow-line AGNs is based on the

permitted $H\beta$ and $H\alpha$ lines.

The studied narrow-line RASS/SDSS AGNs are found to have, on average, lower observed X-ray luminosities than broad-line RASS/SDSS AGNs. However, the vast majority of broad-line RASS/SDSS AGNs are known to be unabsorbed X-ray sources, therefore, their observed X-ray luminosity is equal to their intrinsic X-ray luminosity. On the other hand, narrow-line RASS/SDSS AGNs may be absorbed AGNs and their intrinsic X-ray luminosities could be higher than the observed ones given in Figure 4. Consequently, both classes of RASS/SDSS AGN samples may be very similar with respect to intrinsic X-ray luminosity.

Due to *ROSAT*'s soft energy range of 0.1–2.4 keV, narrow-line RASS/SDSS AGNs can be absorbed only by moderate column densities (N_H). We simulate an X-ray spectrum with a photon index of $\Gamma = 2.5$, galactic absorption of $N_{H,gal} = 2 \times 10^{20} \text{ cm}^{-2}$, and a typical redshift of $z = 0.15$, in order to estimate which intrinsic N_H values are detectable with *ROSAT*. Compared to an unabsorbed source, the flux in the 0.1–2.4 keV *ROSAT* band drops down to 61% when an intrinsic column density of $N_H = 10^{21} \text{ cm}^{-2}$ is used (21% for $N_H = 10^{22} \text{ cm}^{-2}$). We conclude that only objects with $N_H \lesssim 10^{22} \text{ cm}^{-2}$ are detected in the RASS. Most likely the narrow-line RASS/SDSS AGN sample consists mainly of a mixture of unabsorbed and only moderately absorbed (a few $N_H = 10^{21} \text{ cm}^{-2}$) AGNs.

Although broad-line AGNs have a much lower projected space density than narrow-line AGNs and therefore yield, in general, more reliable identification with the RASS counterpart, Anderson et al. (2003, 2007) successfully demonstrate that the narrow-line RASS/SDSS AGN are statistically very reliable identifications as well. They estimate that less than 5% of the counterparts are spurious random chance positional coincidences. Convincing evidence derives from the distribution of positional offsets relative to the X-ray positional error and equal area annuli. Furthermore, the observed distribution of the ratios of RASS/SDSS X-ray-to-optical flux matches expectations for typical X-ray emitting AGNs. For details see Anderson et al. (2003, 2007). We conclude that the narrow-line RASS/SDSS AGNs have a comparable high counterpart reliability as the broad-line RASS/SDSS AGNs.

In the redshift range of $0.07 < z < 0.16$ 31 out of 194 narrow-line RASS/SDSS AGNs are also classified as SDSS main galaxies, while at $0.16 < z < 0.36$ only one object belongs to the narrow-line RASS/SDSS AGN sample and the LRG tracer set. As for the broad-line RASS/SDSS AGNs, we create a SDSS main galaxy sample that does not include galaxies that have been also classified as narrow-line RASS/SDSS AGNs and compute the corresponding CCF. On scales greater than $5 h^{-1} \text{ Mpc}$, the pair counts differ by less than 0.1% from the original CCF. Therefore, the overlap in the samples does not affect the clustering results for the narrow-line RASS/SDSS AGNs.

3.2. Optically-selected SDSS Samples

All of our optically-selected SDSS AGNs (called ‘quasars’ in the SDSS literature) are drawn from Schneider et al. (2010) and use the full SDSS survey

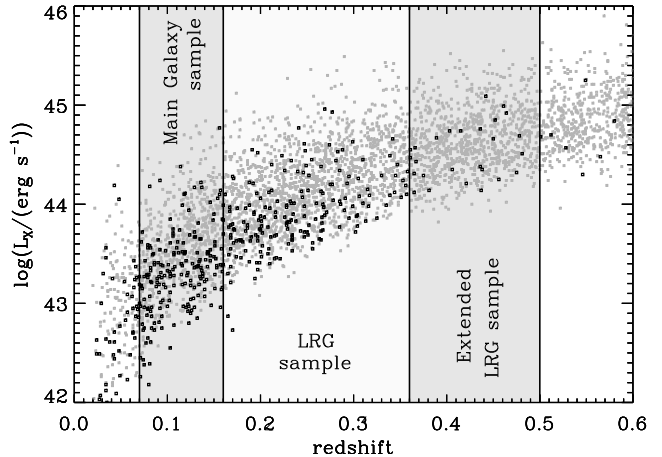


FIG. 4.— Location of narrow-line RASS/SDSS AGNs (black squares) in the 0.1–2.4 keV observed X-ray luminosity versus redshift plane for the studied DR4+ X-ray samples. Gray dots show broad-line RASS/SDSS AGNs. The filled areas illustrate the redshift ranges of the different samples used here.

(DR7). The AGN candidate selection is described in detail in Richards et al. (2002) and can be summarized as follows. The highest priority is given to FIRST-detected optical point sources. Then sources with non-stellar colors in the *ugriz* photometry data are considered. Objects with photometric redshifts of $z \lesssim 3$ are targeted even if they are spatially resolved. FIRST-detected optical point sources and $z \lesssim 3$ AGN candidates are required to have a Galactic extinction-corrected *i* magnitude of 19.1. This selection method picks ~ 18 objects per square degree which are followed up with the SDSS spectrograph. The resulting ‘primary’ SDSS AGN sample is then supplemented by objects targeted by other SDSS spectroscopic selections (main galaxies, LRGs, RASS, stars, and serendipitous sources) that turned out to be AGNs. In the redshift range of interest ($0.07 < z < 0.50$), these secondary channels account for $\sim 9\%$ of the total SDSS AGN sample (vast majority from the galaxy target selection). If a significant number of SDSS AGNs from these secondary channels were originally selected from the LRG sample, which is known to be strongly clustered, it could bias the AGN clustering. We verified that there is no overlap between the SDSS AGN and the LRG sample. Therefore, we do not expect any influences on our AGN clustering measurements caused by the secondary selection channel.

Schneider et al. (2010) (and references within) have constructed AGN catalogs based on different SDSS data releases. They apply a luminosity selection of $M_i \leq -22$ mag and require that objects have at least one emission line exceeding a FWHM of 1000 km s^{-1} . Objects that have a spectrum with only narrow permitted AGN-typical emission lines are removed. The absolute magnitude M_i is computed by using the *i* PSF Galactic extinction-corrected magnitude measurement and assuming a typical AGN spectral energy slope.

Historically, quasars are defined as objects at the high end of the AGN luminosity function having $M_B \leq -23$ mag (e.g., Schmidt & Green 1983). $M_i = -22$ mag corresponds to $M_B = -22.4$ mag for an typical AGN at $z = 0$. The Schneider et al. SDSS AGN catalog papers use the *i*-band instead of the *B*-band in part because the

i -filter is less affected by Galactic absorption. However, a significant disadvantage of this is that the host galaxy light may represent a larger contribution to the total flux than the AGN. AGNs near the $M_i = -22$ mag cut can be equally bright as the host galaxy, e.g., host galaxies at $z \sim 0.4$ with $i = 19.1$ mag (within the detection limit of the SDSS AGN selection method) have $M_i = -22$ mag. Consequently, these AGNs may be less luminous than their quoted optical magnitude. This effect is somewhat mitigated by the use of the PSF photometric data in the AGN selection but should be kept in mind when interpreting our results.

The AGN candidates selection by Richards et al. (2002) has undergone constant modification to improve the efficiency. Schneider et al. (2010, 2007) use the final selection algorithm. AGNs in these catalogs have two spectroscopic target selection flags: BEST (final algorithm) and TARGET (actual algorithm during targeting). BEST uses the latest photometric software and has the highest quality data. The continuous modification of the AGN selection method and the inclusion of AGNs not selected by the standard selection means that the AGN catalogs are not statistically clean samples. The catalog of Schneider et al. (2010) contains 105,783 spectroscopically confirmed AGNs which have luminosities of $M_i \leq -22$, have at least one emission line exceeding a FWHM of 1000 km s^{-1} , have highly reliable redshifts, and are fainter than $i \sim 15$. We extract only objects that have a MODE flag of 'PRIMARY'. This procedure applies to 99% of all objects and limits our sample to objects that have been spectroscopically followed up based on a target selection and are not blended. We use the BEST flags whenever TARGET and BEST are available. We use optically-selected SDSS AGNs in the redshift ranges of the corresponding tracer sets ($0.07 < z < 0.16$, $0.16 < z < 0.36$, $0.36 < z < 0.50$). Except for the $0.07 < z < 0.16$ AGN sample, where the number of objects is very low, we further subdivide the samples into lower and higher M_i subsamples (see Table 1). The M_i cuts are chosen to yield approximately the same number of objects in the different luminosity subsamples. We use $M_i = -22.4$ for the $0.16 < z < 0.36$ sample and $M_i = -22.9$ for the $0.36 < z < 0.50$ sample (Fig. 5).

In the $0.07 < z < 0.16$ redshift range we find a high overlap between objects derived from the Schneider et al. (2010) AGN sample and the SDSS main galaxy sample. 133 out of 177 SDSS AGNs are also classified as SDSS main galaxies. As with the RASS/SDSS AGNs, we exclude these objects from the SDSS main galaxy sample and compute the CCF. The difference in the CCF occurs only on the larger scales and is less than 1%; therefore the overlap affects the clustering measurements very little. At higher redshifts, there is no overlap between optically-selected SDSS AGN samples and SDSS LRGs used as our tracer sets. For the optically-selected SDSS AGNs we do not estimate the co-moving number densities in Table 1. Their selection function is very complex and requires a sophisticated modeling method, which is beyond the scope of this paper.

3.2.1. Radio-quiet Optically-selected SDSS AGN Samples

To test the impact of radio-loud AGNs on the clustering signal of optically-selected AGN samples, we further exclude FIRST radio-detected objects in the

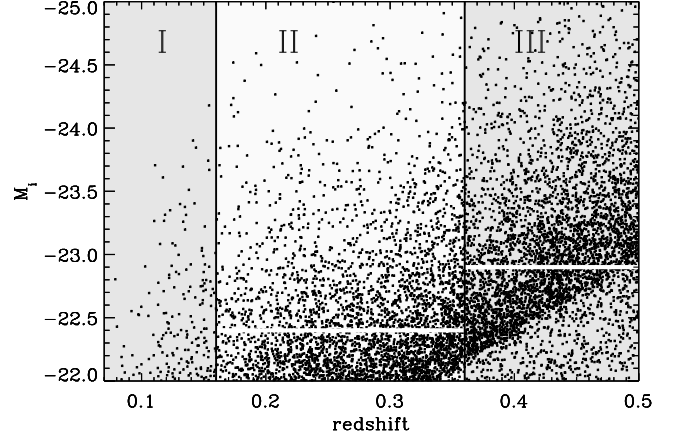


FIG. 5.— Absolute magnitude M_i vs. redshift for optically-selected broad-line SDSS DR7 AGNs from Schneider et al. (2010). The vertical black lines illustrate the redshift ranges of the different AGN samples and tracer sets, following Figs. 2 and 4. The white horizontal solid lines show the cut used to create lower and higher M_i optically-selected SDSS AGN subsamples.

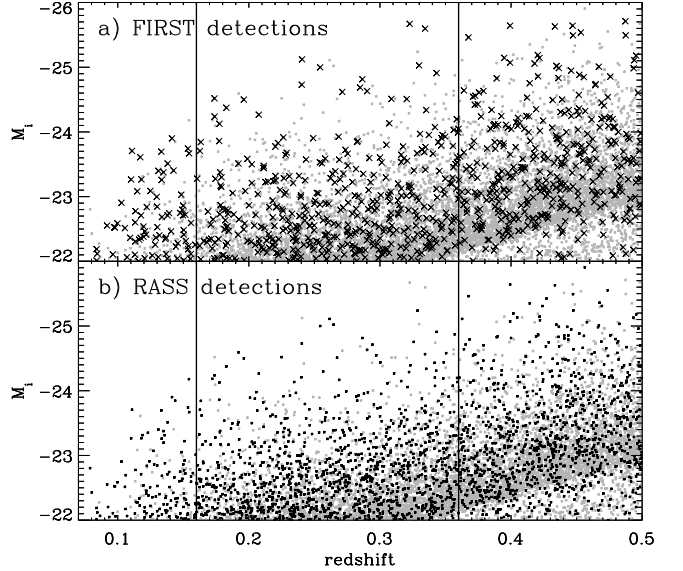


FIG. 6.— Similar to Figure 5, here showing the location of optically-selected broad-line FIRST-detected AGNs (top panel, crosses) and RASS-detected AGNs (lower panel, asterisks) in the absolute M_i -magnitude-redshift plane. In the top panel we select only objects that fall in regions covered by FIRST and SDSS. The solid vertical lines show the different redshift ranges of the samples.

Schneider et al. (2010) AGN samples. An AGN has a radio detection if its position coincides with a FIRST catalog entry within 2 arcsec. We restrict all samples to the FIRST area to ensure that no radio-loud AGN is selected for the radio-quiet samples. Then we remove objects that have a measured FIRST radio flux in the AGN catalog. This is the same conservative approach of excluding all FIRST-detected AGNs as we do in Sect. 3.1.1 for the radio-quiet RASS/SDSS AGN subsamples. Here we also use our definition of radio-quiet AGN samples for the optically selected AGNs, namely that radio-to-optical flux density R based on the FIRST is $R = 0$. We also account for the restriction to the FIRST geometry in the corresponding tracer sets when we derive the ACF of the radio-quiet optically-selected AGN samples. The resulting samples are labeled with the subsequent entry

‘(rq)’ in Tables 1, 2, and 3.

Figure 6 (top panel) shows the distribution of optically-selected FIRST-detected AGNs within the larger optically-selected AGN sample. A fraction of 44% of the $0.07 < z < 0.16$ AGNs, 13% of $0.16 < z < 0.36$ AGNs, and 9% of the $0.36 < z < 0.50$ AGNs are detected by FIRST (considering only regions that are covered by FIRST and SDSS). The fraction is a sensitive function of redshift, as it depends on luminosity. The higher M_i subsamples contain more FIRST radio-detections (17% in $0.16 < z < 0.36$ and 12% in $0.36 < z < 0.50$) than the lower M_i subsamples (8% in $0.16 < z < 0.36$ and 5% in $0.36 < z < 0.50$). 78 out of the 96 radio-quiet SDSS AGN in the redshift range $0.07 < z < 0.16$ are also classified as SDSS main galaxies.

3.2.2. X-ray selected Optical AGN Samples

The large number of X-ray detected optically-selected SDSS AGNs at redshifts above $z = 0.16$ allows us to test how different selections of AGNs affect the clustering signal of broad-line AGNs. The catalog paper by Schneider et al. (2010) lists for each individual AGN the relevant information if the object has a detection in the RASS faint or bright source catalog. Beside the construction of a radio-quiet optically-selected SDSS AGN sample (Section 3.2.1), we create a sample that contains only optically-selected broad-line SDSS AGNs that are *not* detected in RASS. This sample has the subsequent entry ‘(noX)’ in the corresponding tables. Figure 6 (panel b) shows the distribution of objects with RASS detections among the optically-selected SDSS AGN sample. A fraction of 70% of the optically-selected SDSS AGNs are also detected by RASS in the redshift range of $0.07 < z < 0.16$. At higher redshifts RASS detects 32% ($0.16 < z < 0.36$) and 22% ($0.36 < z < 0.50$) of the optically-selected broad-line SDSS AGNs. This is not surprising, as the low *ROSAT* sensitivity results in the RASS redshift distribution rising quickly to $z \sim 0.15$ and strongly decreasing at higher redshift.

The optical and X-ray luminosities of broad emission line AGNs are known to be strongly correlated, the ratio of which is often expressed by the optical-to-X-ray spectral energy index α_{ox} (e.g., Avni & Tananbaum 1986; Green et al. 1995; Steffen et al. 2006; Krumpe et al. 2007; Anderson et al. 2007). Therefore, RASS detects 44% of the AGNs in the higher M_i sample at $0.16 < z < 0.36$ (29% at $0.36 < z < 0.50$) but only 24% of the AGNs in the lower M_i sample at $0.16 < z < 0.36$ (17% at $0.36 < z < 0.50$).

RASS contains only the highest flux X-ray emitting AGNs but has the complementary advantage of detecting lower AGN activity compared to the optically-selected broad-line SDSS AGNs. X-ray luminosities of $\log(L_X/[\text{ergs}^{-1}]) > 42$ are a clear indicator of AGN activity, while in the optical a strong starlight component from the host galaxy can make it difficult to detect broad-line AGNs. The location of the RASS-detected AGNs in Fig. 6 (panel b) indicates that RASS extends the detections of broad-line AGNs below the optical cut of $M_i = -22$ mag used by Schneider et al. (2010) at $z \lesssim 0.35$.

Furthermore, we also create AGN samples that contain only optically-selected SDSS AGN that are also detected as RASS sources (Fig. 6, panel b). The samples

are labeled with the subsequent entry ‘(onlyX)’. For these object we have both the X-ray and optical luminosities (L_X, M_i). In general, as expected by the α_{ox} connection, high/low M_i corresponds to high/low L_X . The fraction of FIRST-detected AGNs increases more with M_i than with L_X .

Finally, we design samples of optically-selected SDSS AGNs that are neither FIRST nor RASS detections. These samples only cover the FIRST area. This selection results in 56% of the $0.16 < z < 0.36$ and 67% of the $0.36 < z < 0.50$ optically-selected SDSS AGNs. We refer to these samples by the subsequent entry ‘(rq+noX)’.

4. CLUSTERING ANALYSIS

We measure the two-point correlation function $\xi(r)$ (Peebles 1980), which measures the excess probability dP above a Poisson distribution of finding an object in a volume element dV at a distance r from another randomly chosen object. The auto-correlation function (ACF) measures the spatial clustering of objects in the same sample, while the cross-correlation function (CCF) measures the clustering of objects in two different samples. We use the same approach as described in detail in paper I (Section 3). Here we reiterate the essential elements of our method.

We use the correlation estimator of Davis & Peebles (1983) in the form

$$\xi(r) = \frac{DD(r)}{DR(r)} - 1, \quad (2)$$

where $DD(r)$ is the number of data-data pairs with a separation r , and $DR(r)$ is the number data-random pairs; both pair counts have been normalized by the number density of data and random points. We measure ξ on a two-dimensional grid of separations r_p , perpendicular to the line of sight, and π , along the line of sight, to separate the effects of redshift space distortion due to peculiar velocities along the line of sight. We obtain the projected correlation function $w_p(r_p)$ by integrating $\xi(r_p, \pi)$ along the π direction.

As in paper I, we infer the AGN ACF from the CCF between AGNs and corresponding galaxy tracer set and the ACF of the tracer set using Coil et al. (2009):

$$w_p(\text{AGN}|\text{AGN}) = \frac{[w_p(\text{AGN}|\text{TRACE})]^2}{w_p(\text{TRACE}|\text{TRACE})}, \quad (3)$$

where $w_p(\text{AGN}|\text{AGN})$, $w_p(\text{TRACE}|\text{TRACE})$ are the ACFs of the AGN and the corresponding tracer set, respectively, and $w_p(\text{AGN}|\text{TRACE})$ is the CCF of the AGNs with the tracer set. In other words, we assume that the CCF is the geometric mean of two ACFs, which has been verified to be valid by Zehavi et al. (2011) (Appendix A).

The CCF is computed by applying Eq. 2

$$\xi_{\text{AGN-TRACE}} = \frac{D_{\text{AGN}} D_{\text{TRACE}}}{D_{\text{AGN}} R_{\text{TRACE}}} - 1. \quad (4)$$

For our purposes, the use of this simple estimator has several major advantages and results in only a marginal loss in the signal-to-noise ratio when compared to more advanced estimators (e.g., Landy & Szalay 1993). The estimator in Eq. 4 requires the generation of a random

catalog only for the tracer set. The tracer sets have well-defined selection functions and are, except for the extended LRG sample, volume-limited. Since the random catalog should exactly match all observational biases to minimize the systematic uncertainties, well understood selection effects are a key to generation proper random samples. The AGN samples suffer from very complex and hard to model selection functions. Therefore, a random catalog of X-ray selected RASS/SDSS AGN is subject to large systematic uncertainties due to the difficulty in accurately modeling the position-dependent sensitivity limit and the variation in the flux limit of the sources (caused by changing Galactic absorption over the sky and spectrum-dependent corrections). Optically-selected SDSS AGNs (see Section 3.2) rely on constantly modified selection algorithms and the acceptance of additional incomplete AGN selection methods. Consequently, the modeling of their selection function for the generation of a random catalog would be very challenging.

The errors in the adjacent bins in correlation measurements are not independent. Poisson errors will significantly underestimate the uncertainties and should not be used for error calculations. Instead, we use the jackknife resampling technique to estimate the measurement errors as well as the covariance matrix M_{ij} , which reflects the degree to which bin i is correlated with bin j . The covariance matrix is used to obtain reliable power law fits to $w_p(r_p)$ by minimizing the correlated χ^2 values. In our jackknife resampling, we divide the survey area into $N_T = 100$ subsection for the DR4+ geometry and 131 subsections for DR7, each of which is ~ 50 – 60 deg². These N_T jackknife-resampled correlation functions define the covariance matrix (Eq. 5):

$$M_{ij} = \frac{N_T - 1}{N_T} \left[\sum_{k=1}^{N_T} \left(w_k(r_{p,i}) - \langle w(r_{p,i}) \rangle \right) \times \left(w_k(r_{p,j}) - \langle w(r_{p,j}) \rangle \right) \right] \quad (5)$$

We calculate $w_p(r_p)$ N_T times, where each jackknife sample excludes one section and $w_k(r_{p,i})$ and $w_k(r_{p,j})$ are from the k -th jackknife samples of the AGN ACF and $\langle w(r_{p,i}) \rangle$, $\langle w(r_{p,j}) \rangle$ are the averages over all of the jackknife samples. The uncertainties represent a 1σ (68.3%) confidence interval.

The generation of covariance matrix for the inferred AGN ACF considers the N_T jackknife-resampled correlation functions of the CCF (AGN and corresponding tracer set) and the tracer set ACF. For each jackknife sample we calculate the inferred AGN ACF by using Equation 3. The resulting N_T $w_p(r_p)$ jackknife-resampled projected correlation functions of the inferred ACFs are then used to compute the covariance matrix of the inferred AGN ACF.

4.1. Inferring the AGN Auto-correlation Function

To infer the AGN ACF, we measure the CCF of the AGN sample with the tracer set and the ACF of the tracer set. In both cases we measure r_p in a range of 0.05 – 40 h^{-1} Mpc in 15 bins in a logarithmic scale. The upper 11 bins are identical with the bins used in paper I and cover the r_p range of 0.3 – 40 h^{-1} Mpc. Consequently, we extend the measurements by four additional bins to

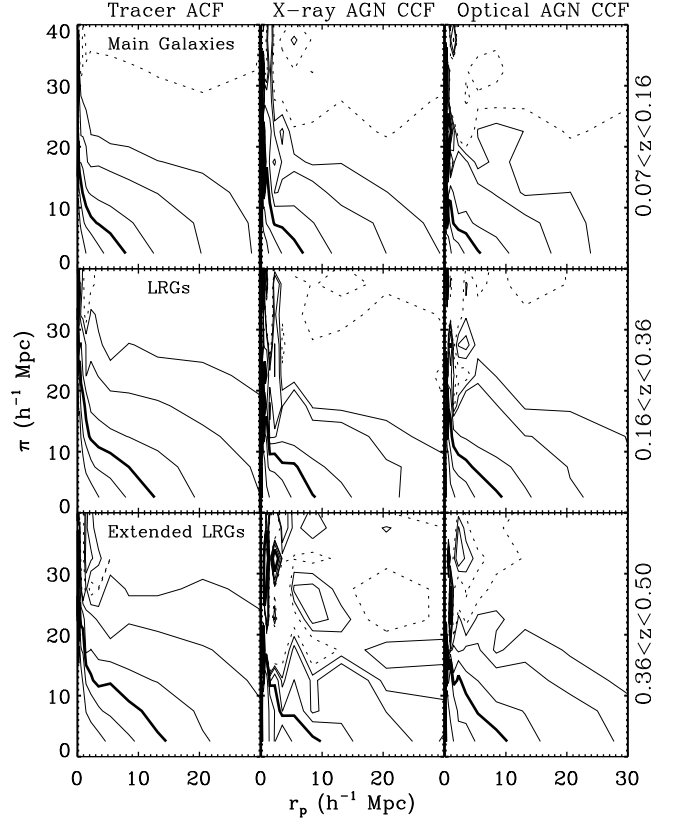


FIG. 7.— Contour plots of the auto-correlation functions $\xi(r_p, \pi)$ of the different tracer sets (left panels, top – SDSS main galaxies, middle – LRGs, bottom – extended LRGs) and cross-correlation functions of the X-ray selected (RASS/SDSS) AGN samples (middle panels) and the optically-selected SDSS AGNs (right panels) with the corresponding tracer set. The shown CCFs use in all cases the total AGN sample in the corresponding redshift range. In the π direction we use a binning of 5 h^{-1} Mpc. Contour lines show constant correlation strength for the two-dimensional correlation function $\xi(r_p, \pi)$. The contour levels are 0.0 (dotted line), 0.1 , 0.2 , 0.5 , 1.0 (thick solid line), 2.0 , and 5.0 .

smaller scales. We compute π in steps of 5 h^{-1} Mpc in a range of $\pi = 0$ – 200 h^{-1} Mpc. The resulting $\xi(r_p, \pi)$ are shown in Fig. 7 for the ACF of the tracer sets and for the CCF of the total AGN samples (X-ray & optically-selected) with the corresponding tracer sets.

Although the projected correlation function is computed by integrating over π to infinity (see paper I, Equations 5, 11), in practice an upper bound of the integration (π_{\max}) is used to include most of the correlated pairs, give stable solutions, and suppress the noise introduced by distant, uncorrelated pairs. We compute $w_p(r_p)$ for a set of π_{\max} ranging from 10 – 160 h^{-1} Mpc in steps of 10 h^{-1} Mpc. We then fit $w_p(r_p)$ over a r_p range of 0.3 – 40 h^{-1} Mpc with a fixed $\gamma = 1.9$ and determine the correlation length r_0 for the individual π_{\max} measurements. As in paper I, we find that the LRG ACFs (LRG sample and extended LRG sample) saturate at $\pi_{\max} = 80$ h^{-1} Mpc. All CCFs and the main galaxy sample ACFs saturate at $\pi_{\max} = 40$ h^{-1} Mpc. In addition, above these values the corresponding correlation lengths do not change by more than 1σ , considering the increased uncertainties with increasing π_{\max} values. The use of $\pi_{\max} = 80$ h^{-1} Mpc for the LRG ACFs and $\pi_{\max} = 40$ h^{-1} Mpc for the main galaxy ACFs and all CCFs matches the

π_{\max} values used for these samples by other studies, e.g., Zehavi et al. (2005a) (LRG) and Zehavi et al. (2005b) (SDSS galaxies). The $w_p(r_p)$ CCFs for the different total AGN samples with the corresponding tracer sets are shown in Fig. 8, while the resulting power law fits for the ACFs and CCFs based on

$$w_p(r_p) = r_p \left(\frac{r_0}{r_p} \right)^\gamma \frac{\Gamma(1/2)\Gamma((\gamma-1)/2)}{\Gamma(\gamma/2)}, \quad (6)$$

where $\Gamma(x)$ is the Gamma function, are listed in Table 2.

Our values for the ACFs of the tracer sets agree well with measurements from other studies. Using a slightly different magnitude cut of $-22 < M_r < -21$ in the redshift range $0.07 < z < 0.16$, Zehavi et al. (2005b) find for the SDSS DR2 main galaxy sample a correlation length of $r_0 = 6.16 \pm 0.17 h^{-1}$ Mpc and a slope of $\gamma = 1.85 \pm 0.03$, fitting over the range $r_p = 0.13 - 20 h^{-1}$ Mpc. Zehavi et al. (2005a) study the clustering of $\sim 30,000$ LRGs with $-23.2 < M_g^{0.3} < -21.2$ and measure $r_0 = 9.80 \pm 0.20 h^{-1}$ Mpc and a slope of $\gamma = 1.94 \pm 0.02$, fitting over the range $r_p = 0.3 - 30 h^{-1}$ Mpc. Their clustering measurement in a sample of high luminosity LRGs ($-23.2 < M_g^{0.3} < -21.8$, $0.16 < z < 0.44$) yields $r_0 = 11.21 \pm 0.24 h^{-1}$ Mpc and $\gamma = 1.92 \pm 0.03$.

In Table 3 we list the redshift range, the median effective redshift of $N_{\text{CCF}}(z)$ for the corresponding AGN samples, the derived best r_0 and γ values based on power law fits, and r_0 for a power law fit with a fixed slope of $\gamma = 1.9$. The data are fitted over the range $r_p = 0.3 - 15 h^{-1}$ Mpc to be consistent with paper I. Since we measure the CCF to infer the ACF, the resulting effective redshift distribution for the clustering signal is determined by both the redshift distribution of the tracer set and the AGN sample: $N_{\text{CCF}}(z) = N_{\text{tracer}}(z) * N_{\text{AGN}}(z)$.

The clustering strength is commonly expressed in terms of the rms fluctuations within a sphere with a co-moving radius of $8 h^{-1}$ Mpc ($\sigma_{8,\text{AGN}}$, see Equation 13 in paper I). We derive $\sigma_{8,\text{AGN}}$ from the best fit parameters of the power law fits. The uncertainties on $\sigma_{8,\text{AGN}}$ are derived from the r_0 versus γ confidence contours of the one-parameter fit based on a correlated $\chi^2 = \chi^2_{\min} + 1.0$. Using $\sigma_{8,\text{AGN}}$, we further derive the bias parameter $b = \sigma_{8,\text{AGN}}(z)/\sigma_8(z)$ based on our power law fits and give these values in column ‘ $b(z)$ PL-fits’ of Table 3. The parameter b indicates the clustering strength by comparing the observed AGN clustering to that of the underlying mass distribution from linear growth theory (Hamilton 2001), with $\sigma_8(z) = D(z)\sigma_8(z=0)$, where $D(z) = D_1(z)/D_1(z=0)$ is the linear growth factor (Section 7.5 in Dodelson 2003). We use $\sigma_8(z=0) = 0.8$ (see Section 1). The bias quantifies the amplification factor of the contrast of the object distribution with respect to that of the dark matter density distribution. The uncertainties of b are derived from the standard deviation of $\sigma_{8,\text{AGN}}$.

Column ‘ $b(z)$ HOD’ of Table 3 lists the bias parameter derived using halo occupation distribution (HOD) modeling, which is described below in Section 5. Using Equation 8 of Sheth et al. (2001) and the improved fit for this equation given by Tinker et al. (2005), we compute the expected large-scale Eulerian bias factor for different DMH masses at different redshifts. Com-

TABLE 2
POWER LAW FITS TO THE ACFs OF THE TRACER SETS AND THE CCFs OF THE AGN – TRACER SETS

Sample Name	Redshift Range	r_0 (h^{-1} Mpc)	γ
SDSS Tracer Sets			
main galaxy (DR4+)	0.07 – 0.16	$6.30^{+0.12}_{-0.12}$	$1.85^{+0.02}_{-0.02}$
main galaxy (DR7)	0.07 – 0.16	$6.27^{+0.12}_{-0.12}$	$1.84^{+0.02}_{-0.02}$
LRG (DR4+)	0.16 – 0.36	$9.63^{+0.14}_{-0.14}$	$1.98^{+0.02}_{-0.02}$
LRG (DR7)	0.16 – 0.36	$9.54^{+0.13}_{-0.13}$	$1.95^{+0.02}_{-0.02}$
extended LRG (DR4+)	0.36 – 0.50	$10.90^{+0.24}_{-0.24}$	$1.91^{+0.03}_{-0.03}$
extended LRG (DR7)	0.36 – 0.50	$10.87^{+0.19}_{-0.19}$	$1.89^{+0.03}_{-0.02}$
X-ray Selected AGN – RASS/SDSS AGN			
total RASS-AGN	0.07 – 0.16	$5.79^{+0.24}_{-0.25}$	$1.84^{+0.05}_{-0.05}$
total RASS-AGN(rq)	0.07 – 0.16	$5.78^{+0.27}_{-0.27}$	$1.86^{+0.05}_{-0.05}$
low L_X RASS-AGN	0.07 – 0.16	$5.19^{+0.34}_{-0.36}$	$1.96^{+0.10}_{-0.09}$
high L_X RASS-AGN	0.07 – 0.16	$6.07^{+0.34}_{-0.35}$	$1.79^{+0.06}_{-0.06}$
low L_X RASS-AGN (rq)	0.07 – 0.16	$5.49^{+0.35}_{-0.36}$	$1.94^{+0.09}_{-0.09}$
high L_X RASS-AGN (rq)	0.07 – 0.16	$6.06^{+0.42}_{-0.44}$	$1.79^{+0.06}_{-0.06}$
narrow line RASS-AGN	0.07 – 0.16	$4.99^{+0.45}_{-0.48}$	$1.82^{+0.12}_{-0.10}$
total RASS-AGN	0.16 – 0.36	$6.88^{+0.27}_{-0.28}$	$1.85^{+0.04}_{-0.04}$
total RASS-AGN(rq)	0.16 – 0.36	$7.01^{+0.29}_{-0.29}$	$1.86^{+0.05}_{-0.05}$
low L_X RASS-AGN	0.16 – 0.36	$6.22^{+0.36}_{-0.38}$	$1.85^{+0.07}_{-0.06}$
high L_X RASS-AGN	0.16 – 0.36	$7.50^{+0.38}_{-0.41}$	$1.90^{+0.07}_{-0.07}$
low L_X RASS-AGN (rq)	0.16 – 0.36	$6.09^{+0.37}_{-0.39}$	$1.85^{+0.07}_{-0.06}$
high L_X RASS-AGN (rq)	0.16 – 0.36	$7.83^{+0.39}_{-0.41}$	$1.94^{+0.08}_{-0.08}$
narrow line RASS-AGN	0.16 – 0.36	$5.78^{+0.74}_{-0.86}$	$1.77^{+0.14}_{-0.14}$
total RASS-AGN	0.36 – 0.50	$6.82^{+0.42}_{-0.44}$	$1.97^{+0.10}_{-0.09}$
total RASS-AGN(rq)	0.36 – 0.50	$6.67^{+0.44}_{-0.49}$	$2.08^{+0.11}_{-0.11}$
Optically-selected AGN – SDSS AGN			
total SDSS-AGN	0.07 – 0.16	$4.93^{+0.41}_{-0.43}$	$1.98^{+0.12}_{-0.11}$
total SDSS-AGN(rq)	0.07 – 0.16	$4.70^{+0.53}_{-0.58}$	$2.11^{+0.17}_{-0.14}$
total SDSS-AGN	0.16 – 0.36	$6.91^{+0.17}_{-0.18}$	$1.91^{+0.04}_{-0.04}$
total SDSS-AGN(rq)	0.16 – 0.36	$6.98^{+0.20}_{-0.20}$	$1.88^{+0.04}_{-0.04}$
total SDSS-AGN (noX)	0.16 – 0.36	$6.93^{+0.21}_{-0.22}$	$1.93^{+0.04}_{-0.04}$
total SDSS-AGN (rq+noX)	0.16 – 0.36	$6.96^{+0.23}_{-0.23}$	$1.89^{+0.05}_{-0.04}$
total SDSS-AGN (onlyX)	0.16 – 0.36	$7.10^{+0.32}_{-0.33}$	$1.85^{+0.05}_{-0.05}$
low M_i SDSS-AGN	0.16 – 0.36	$6.91^{+0.24}_{-0.25}$	$1.91^{+0.05}_{-0.05}$
high M_i SDSS-AGN	0.16 – 0.36	$6.74^{+0.22}_{-0.22}$	$1.90^{+0.05}_{-0.05}$
low M_i SDSS-AGN (rq)	0.16 – 0.36	$6.88^{+0.26}_{-0.26}$	$1.90^{+0.05}_{-0.05}$
high M_i SDSS-AGN (rq)	0.16 – 0.36	$6.91^{+0.27}_{-0.28}$	$1.87^{+0.05}_{-0.05}$
total SDSS-AGN	0.36 – 0.50	$7.21^{+0.21}_{-0.22}$	$1.87^{+0.04}_{-0.04}$
total SDSS-AGN (rq)	0.36 – 0.50	$7.24^{+0.22}_{-0.23}$	$1.91^{+0.04}_{-0.04}$
total SDSS-AGN (noX)	0.36 – 0.50	$7.02^{+0.24}_{-0.25}$	$1.81^{+0.04}_{-0.04}$
total SDSS-AGN (rq+noX)	0.36 – 0.50	$7.08^{+0.25}_{-0.26}$	$1.84^{+0.04}_{-0.04}$
low M_i SDSS-AGN	0.36 – 0.50	$7.12^{+0.30}_{-0.31}$	$1.91^{+0.06}_{-0.06}$
high M_i SDSS-AGN	0.36 – 0.50	$6.96^{+0.33}_{-0.36}$	$1.81^{+0.07}_{-0.07}$
low M_i SDSS-AGN (rq)	0.36 – 0.50	$7.12^{+0.32}_{-0.34}$	$1.95^{+0.06}_{-0.06}$
high M_i SDSS-AGN (rq)	0.36 – 0.50	$7.16^{+0.33}_{-0.36}$	$1.84^{+0.06}_{-0.06}$

NOTE. — Values of r_0 and γ obtained from a power law fit to $w_p(r_p)$ over the range $r_p = 0.3 - 40 h^{-1}$ Mpc for all samples using the full covariance matrix. For the LRG and extended LRG ACFs, we use $\pi_{\max} = 80 h^{-1}$ Mpc, while for all other ACFs and CCFs we use $\pi_{\max} = 40 h^{-1}$ Mpc. See Table 1 for the definition of the samples.

paring the observed b value from HOD modeling with the DMH bias factor from Λ CDM cosmological simulations provides an estimate of the typical DMH mass ($b_{\text{DMH}}(M_{\text{DMH}}^{\text{typ}}) = b_{\text{OBS,HOD}}$) in which the different AGN samples reside, listed in the last column of Table 3.

4.2. Robustness of the Clustering Measurements

In this section, we verify the stability of our result against possible observational biases and systematic effects. As shown in paper I, the somewhat non-contiguous coverage of the SDSS DR4+ survey does not influence the clustering results significantly, given the uncertainties. For DR7 the situation improves as the SDSS geometry is much more contiguous. We verify that the number of random points is large enough to lead to a high number of pair counts at the smallest scales measured and not introduce noise.

Zehavi et al. (2005b) note that the largest structure detected in SDSS (the Sloan Great Wall) influences the galaxy clustering significantly for samples with $M_r^{0.1} < -21$ and $z < 0.1$. Therefore, we explore this effect on our SDSS main galaxy sample. We measure the ACF for a main galaxy sample that excludes the Sloan Great Wall ($165 < RA < 210$ and $-5 < Dec < 5$). We find a correlation length of $r_0 = 6.35 \pm 0.12 h^{-1}$ Mpc and $\gamma = 1.83 \pm 0.02$, which agrees well with the clustering measurements in which the Sloan Great Wall is included (see Table 2). We conclude that our main galaxy ACFs and the CCFs using the main galaxy sample as a tracer set are not affected by this supercluster at $z \sim 0.08$.

For several of the AGN subsamples split by luminosity, we have tested that slightly changing the luminosity cuts by up to ± 0.2 mags (both brighter and fainter) does not significantly change the measured CCFs. The combination of the different tests listed above provides convincing evidence that our results are not significantly influenced by systematic effects and demonstrates their robustness.

5. BIAS FROM THE HOD MODELING

In paper II, we develop a novel method to infer the halo occupation distribution (HOD) of RASS/SDSS AGNs directly from the well-constrained cross-correlation function of RASS/SDSS AGNs with LRGs. The results from paper II show that the linear bias parameters and typical DMH masses derived from the best power law fits down to $r_p \approx 0.3 h^{-1}$ Mpc are subject to systematic errors. This is mainly because the power law fits include scales in the non-linear regime ($r_p \lesssim 1.5 h^{-1}$ Mpc), where the contribution from pairs of objects that belong to the same DMH (the one halo term) is substantial. In this non-linear regime the bias-DMH mass relation based on linear theory, in principle, should not be applied. Another, less significant source of systematic error is that even in the linear regime ($r_p \gtrsim 1.5 h^{-1}$ Mpc), the underlying matter correlation function deviates from a power law. In order to avoid these issues, Allevato et al. (2011) derive the bias parameters of their AGN samples in the XMM-COSMOS survey by modeling their AGN ACFs at $r_p \gtrsim 1.5 h^{-1}$ Mpc with $b_{\text{AGN}}^2 \epsilon_{\text{DM}}^{2-h}$, where b_{AGN} is the AGN bias parameter and $\epsilon_{\text{DM}}^{2-h}$ is the two halo term of the dark matter correlation function modeled as the Fourier Transform of the linear power spectrum.

In this paper, instead, we use the HOD modeling de-

veloped in paper II to derive the bias parameter down to $r_p \gtrsim 0.7 h^{-1}$ Mpc, instead of limiting ourselves to $r_p \gtrsim 1.5 h^{-1}$ Mpc. This allows for better constraints on b_A , especially in cases where the two halo dominated (linear) regime extends below $r_p \approx 1.5 h^{-1}$ Mpc, and a better treatment of the cases where the one halo term contribution is still important at $r_p \gtrsim 1.5 h^{-1}$ Mpc. Thus, in our approach, the main constraints are derived from the two halo term, while including the one halo term contribution in the model serves as a first-order perturbation from linear theory.

Paper II discusses the HOD modeling of the CCF between RASS/SDSS AGNs and LRGs at $0.16 < z < 0.36$ for three different models: in model A all AGNs are satellites within the same DMH as the LRGs, while models B and C include different realizations of the cases where central and satellite AGNs are included and explicitly parameterized. See paper II for details of these models. We repeat this exercise here for the AGN samples used in this paper to derive their bias parameters. The detailed results of the extensive HOD modeling will be presented in a separate paper (Miyaji et al. in preparation), where a number of new improvements in the modeling over that presented in paper II will be included. In this paper, we follow exactly the method presented in paper II. Here we reiterate the main procedure:

1. Determine the central and satellite HODs of the tracer set galaxies ($\langle N_{G,c} \rangle(M_h)$ and $\langle N_{G,s} \rangle(M_h)$, respectively) from their ACF. The space density constraint is additionally used for volume-limited samples (the SDSS main galaxy and the LRG sample).
2. Using the derived tracer set HODs ($\langle N_{G,c} \rangle(M_h)$ & $\langle N_{G,s} \rangle(M_h)$) and using a parameterized model of the AGN central and satellite HODs ($\langle N_{A,c} \rangle(M_h)$ & $\langle N_{A,s} \rangle(M_h)$), we fit the measured CCF between the AGN sample and the tracer set to constrain the AGN HODs. Since the galaxy ACFs have much higher statistical accuracy, the uncertainties in the tracer set HODs are negligible compared to the AGN HOD constraints.
3. Derive the bias parameter of the AGN sample using:

$$b_A = \frac{\int b_h(M_h) \langle N_A \rangle(M_h) \phi(M_h) dM_h}{\int \langle N_A \rangle(M_h) \phi(M_h) dM_h}, \quad (7)$$

where $\langle N_A \rangle(M_h) = \langle N_{A,c} \rangle(M_h) + \langle N_{A,s} \rangle(M_h)$, $b_h(M_h)$ is the bias of DMHs with a mass M_h , and $\phi(M_h)$ is the DMH mass function. We use Equation 8 of Sheth et al. (2001) with parameters from Tinker et al. (2005) for $b_h(M_h)$. The 1σ uncertainties of b_A corresponds to the $\Delta\chi^2 \leq 1$ region in the parameter space of the $\langle N_A \rangle(M_h)$ model.

5.1. The HODs of the tracer sets

5.1.1. SDSS Main Galaxies ($0.07 < z < 0.16$)

As explained above in Section 2.1, the tracer set for the low redshift AGN samples is selected from the SDSS main galaxy sample with an absolute magnitude range of $-22.1 < M_r^{0.1} < -21.1$. The number density of this

TABLE 3
POWER LAW FITS TO THE INFERRED AGN ACF AND DERIVED QUANTITIES.

Sample Name	Redshift Range	Median z_{eff}	r_0 (h^{-1} Mpc)	γ	$r_{0,\gamma=1.9}$ (h^{-1} Mpc)	$b(z)$ PL-fits	$b(z)$ HOD	$\log M_{\text{DMH}}^{\text{typ}}$ ($h^{-1} M_{\odot}$)
X-ray Selected AGN – RASS/SDSS AGN								
total RASS-AGN	0.07 – 0.16	0.13	$4.96^{+0.41}_{-0.44}$	$1.80^{+0.10}_{-0.10}$	$4.84^{+0.38}_{-0.41}$	$1.19^{+0.08}_{-0.09}$	$1.23^{+0.09}_{-0.08}$	$13.22^{+0.13}_{-0.12}$
total RASS-AGN(rq)	0.07 – 0.16	0.14	$4.42^{+0.69}_{-0.77}$	$1.85^{+0.17}_{-0.14}$	$4.33^{+0.62}_{-0.71}$	$1.08^{+0.15}_{-0.17}$	$1.25^{+0.11}_{-0.08}$	$13.24^{+0.14}_{-0.12}$
low L_X RASS-AGN	0.07 – 0.16	0.13	$3.84^{+0.52}_{-0.59}$	$2.10^{+0.23}_{-0.20}$	$3.85^{+0.55}_{-0.63}$	$0.98^{+0.13}_{-0.15}$	$1.11^{+0.11}_{-0.05}$	$13.03^{+0.18}_{-0.09}$
high L_X RASS-AGN	0.07 – 0.16	0.14	$5.35^{+0.65}_{-0.74}$	$1.66^{+0.11}_{-0.12}$	$4.94^{+0.56}_{-0.63}$	$1.25^{+0.12}_{-0.15}$	$1.33^{+0.16}_{-0.14}$	$13.35^{+0.17}_{-0.20}$
low L_X RASS-AGN (rq)	0.07 – 0.16	0.12	$4.18^{+0.77}_{-0.91}$	$2.11^{+0.30}_{-0.23}$	$4.28^{+0.79}_{-0.95}$	$1.07^{+0.19}_{-0.21}$	$1.17^{+0.11}_{-0.08}$	$13.15^{+0.15}_{-0.14}$
high L_X RASS-AGN (rq)	0.07 – 0.16	0.14	$4.67^{+1.07}_{-1.34}$	$1.61^{+0.18}_{-0.17}$	$3.86^{+0.89}_{-1.13}$	$1.10^{+0.22}_{-0.26}$	$1.36^{+0.24}_{-0.18}$	$13.38^{+0.25}_{-0.24}$
narrow line RASS-AGN	0.07 – 0.16	0.13	$3.14^{+0.81}_{-1.23}$	$1.64^{+0.41}_{-0.28}$	$3.10^{+0.70}_{-0.88}$	$0.80^{+0.16}_{-0.23}$	$1.24^{+0.22}_{-0.19}$	$13.24^{+0.22}_{-0.32}$
Optically-Selected AGN – SDSS AGN								
total RASS-AGN	0.16 – 0.36	0.27	$4.05^{+0.43}_{-0.52}$	$1.63^{+0.12}_{-0.12}$	$4.07^{+0.35}_{-0.38}$	$1.06^{+0.09}_{-0.11}$	$1.30^{+0.10}_{-0.08}$	$13.17^{+0.12}_{-0.11}$
total RASS-AGN(rq)	0.16 – 0.36	0.26	$4.50^{+0.46}_{-0.51}$	$1.73^{+0.12}_{-0.12}$	$4.50^{+0.39}_{-0.42}$	$1.16^{+0.11}_{-0.13}$	$1.27^{+0.08}_{-0.08}$	$13.14^{+0.11}_{-0.12}$
low L_X RASS-AGN	0.16 – 0.36	0.24	$3.16^{+0.51}_{-0.70}$	$1.78^{+0.43}_{-0.28}$	$3.18^{+0.42}_{-0.48}$	$0.85^{+0.11}_{-0.13}$	$1.17^{+0.14}_{-0.12}$	$13.01^{+0.21}_{-0.22}$
high L_X RASS-AGN	0.16 – 0.36	0.31	$5.06^{+0.65}_{-0.87}$	$1.82^{+0.17}_{-0.18}$	$5.19^{+0.58}_{-0.65}$	$1.34^{+0.19}_{-0.22}$	$1.48^{+0.12}_{-0.15}$	$13.34^{+0.12}_{-0.17}$
low L_X RASS-AGN (rq)	0.16 – 0.36	0.24	$3.62^{+0.63}_{-0.72}$	$1.85^{+0.37}_{-0.26}$	$3.59^{+0.59}_{-0.70}$	$0.95^{+0.14}_{-0.17}$	$1.18^{+0.14}_{-0.13}$	$13.03^{+0.20}_{-0.24}$
high L_X RASS-AGN (rq)	0.16 – 0.36	0.30	$6.00^{+0.65}_{-0.77}$	$1.97^{+0.18}_{-0.18}$	$5.90^{+0.66}_{-0.74}$	$1.63^{+0.22}_{-0.25}$	$1.50^{+0.20}_{-0.13}$	$13.37^{+0.18}_{-0.14}$
total RASS-AGN	0.36 – 0.50	0.42	$3.24^{+0.96}_{-2.13}$	$1.59^{+0.40}_{-0.41}$	$3.83^{+0.55}_{-0.63}$	$0.96^{+0.22}_{-0.54}$	$1.02^{+0.14}_{-0.09}$	$12.51^{+0.28}_{-0.25}$
total RASS-AGN(rq)	0.36 – 0.50	0.42	$4.13^{+0.81}_{-1.94}$	$1.98^{+0.59}_{-0.56}$	$4.01^{+0.80}_{-0.98}$	$1.20^{+0.34}_{-0.47}$	$0.99^{+0.11}_{-0.06}$	$12.43^{+0.25}_{-0.17}$
Optically-Selected AGN – SDSS AGN								
total SDSS-AGN	0.07 – 0.16	0.14	$3.90^{+0.62}_{-0.70}$	$1.99^{+0.29}_{-0.25}$	$3.94^{+0.62}_{-0.72}$	$0.98^{+0.15}_{-0.17}$	$0.95^{+0.17}_{-0.10}$	$12.67^{+0.37}_{-0.31}$
total SDSS-AGN(rq)	0.07 – 0.16	0.15	$4.16^{+0.85}_{-1.07}$	$2.12^{+0.55}_{-0.39}$	$4.26^{+0.83}_{-1.02}$	$1.08^{+0.20}_{-0.23}$	$0.94^{+0.24}_{-0.13}$	$12.63^{+0.50}_{-0.45}$
total SDSS-AGN	0.16 – 0.36	0.31	$4.80^{+0.24}_{-0.27}$	$1.79^{+0.09}_{-0.09}$	$4.81^{+0.23}_{-0.24}$	$1.26^{+0.07}_{-0.07}$	$1.29^{+0.05}_{-0.05}$	$13.11^{+0.07}_{-0.07}$
total SDSS-AGN(rq)	0.16 – 0.36	0.32	$4.78^{+0.29}_{-0.33}$	$1.72^{+0.10}_{-0.10}$	$4.77^{+0.26}_{-0.27}$	$1.25^{+0.07}_{-0.07}$	$1.31^{+0.08}_{-0.06}$	$13.13^{+0.10}_{-0.09}$
total SDSS-AGN (noX)	0.16 – 0.36	0.32	$4.95^{+0.31}_{-0.32}$	$1.85^{+0.10}_{-0.10}$	$4.94^{+0.30}_{-0.32}$	$1.31^{+0.09}_{-0.09}$	$1.26^{+0.06}_{-0.06}$	$13.06^{+0.08}_{-0.09}$
total SDSS-AGN (rq+noX)	0.16 – 0.36	0.32	$4.80^{+0.33}_{-0.35}$	$1.78^{+0.12}_{-0.11}$	$4.72^{+0.31}_{-0.33}$	$1.27^{+0.07}_{-0.09}$	$1.29^{+0.10}_{-0.07}$	$13.10^{+0.13}_{-0.10}$
total SDSS-AGN (onlyX)	0.16 – 0.36	0.29	$4.70^{+0.50}_{-0.60}$	$1.71^{+0.12}_{-0.12}$	$4.77^{+0.43}_{-0.47}$	$1.22^{+0.12}_{-0.15}$	$1.35^{+0.10}_{-0.11}$	$13.21^{+0.12}_{-0.15}$
low M_i SDSS-AGN	0.16 – 0.36	0.31	$4.73^{+0.36}_{-0.43}$	$1.72^{+0.14}_{-0.13}$	$4.73^{+0.32}_{-0.34}$	$1.23^{+0.09}_{-0.10}$	$1.31^{+0.11}_{-0.09}$	$13.14^{+0.13}_{-0.13}$
high M_i SDSS-AGN	0.16 – 0.36	0.32	$4.36^{+0.35}_{-0.43}$	$1.75^{+0.12}_{-0.12}$	$4.48^{+0.30}_{-0.32}$	$1.17^{+0.08}_{-0.11}$	$1.24^{+0.08}_{-0.08}$	$13.03^{+0.11}_{-0.13}$
low M_i SDSS-AGN (rq)	0.16 – 0.36	0.31	$4.39^{+0.44}_{-0.60}$	$1.65^{+0.15}_{-0.15}$	$4.50^{+0.37}_{-0.37}$	$1.16^{+0.10}_{-0.13}$	$1.30^{+0.09}_{-0.12}$	$13.13^{+0.11}_{-0.18}$
high M_i SDSS-AGN (rq)	0.16 – 0.36	0.32	$4.53^{+0.44}_{-0.56}$	$1.70^{+0.14}_{-0.13}$	$4.64^{+0.37}_{-0.40}$	$1.19^{+0.10}_{-0.13}$	$1.30^{+0.12}_{-0.08}$	$13.12^{+0.14}_{-0.12}$
total SDSS-AGN	0.36 – 0.50	0.42	$4.41^{+0.36}_{-0.44}$	$1.69^{+0.10}_{-0.10}$	$4.58^{+0.29}_{-0.31}$	$1.23^{+0.09}_{-0.11}$	$1.33^{+0.07}_{-0.08}$	$13.05^{+0.09}_{-0.12}$
total SDSS-AGN (rq)	0.36 – 0.50	0.42	$4.66^{+0.36}_{-0.43}$	$1.78^{+0.11}_{-0.11}$	$4.76^{+0.32}_{-0.34}$	$1.30^{+0.09}_{-0.12}$	$1.32^{+0.08}_{-0.08}$	$13.03^{+0.11}_{-0.11}$
total SDSS-AGN (noX)	0.36 – 0.50	0.42	$2.93^{+0.51}_{-0.66}$	$1.39^{+0.10}_{-0.10}$	$3.16^{+0.28}_{-0.30}$	$0.92^{+0.09}_{-0.12}$	$1.42^{+0.08}_{-0.09}$	$13.16^{+0.09}_{-0.11}$
total SDSS-AGN (rq+noX)	0.36 – 0.50	0.42	$3.79^{+0.46}_{-0.58}$	$1.52^{+0.10}_{-0.10}$	$3.80^{+0.32}_{-0.35}$	$1.09^{+0.09}_{-0.11}$	$1.43^{+0.10}_{-0.09}$	$13.17^{+0.11}_{-0.11}$
low M_i SDSS-AGN	0.36 – 0.50	0.40	$4.59^{+0.47}_{-0.61}$	$1.72^{+0.16}_{-0.16}$	$4.70^{+0.40}_{-0.43}$	$1.26^{+0.12}_{-0.15}$	$1.29^{+0.11}_{-0.09}$	$13.02^{+0.14}_{-0.14}$
high M_i SDSS-AGN	0.36 – 0.50	0.43	$2.92^{+0.66}_{-1.02}$	$1.48^{+0.16}_{-0.18}$	$3.42^{+0.38}_{-0.42}$	$0.90^{+0.14}_{-0.19}$	$1.27^{+0.11}_{-0.10}$	$12.95^{+0.15}_{-0.15}$
low M_i SDSS-AGN (rq)	0.36 – 0.50	0.40	$4.68^{+0.48}_{-0.61}$	$1.82^{+0.18}_{-0.17}$	$4.74^{+0.45}_{-0.49}$	$1.31^{+0.14}_{-0.17}$	$1.26^{+0.13}_{-0.12}$	$12.97^{+0.18}_{-0.19}$
high M_i SDSS-AGN (rq)	0.36 – 0.50	0.44	$3.59^{+0.61}_{-0.92}$	$1.56^{+0.16}_{-0.17}$	$3.87^{+0.42}_{-0.47}$	$1.05^{+0.14}_{-0.19}$	$1.35^{+0.12}_{-0.10}$	$13.05^{+0.14}_{-0.14}$

NOTE. — Values of r_0 , γ , and $r_{0,\gamma=1.9}$ are obtained from a fit to $w_p(r_p)$ over the range $r_p = 0.3\text{--}15 h^{-1}$ Mpc for all samples using the full error covariance matrix and minimizing the correlated χ^2 values. The given bias parameters, $b = \sigma_{8,\text{AGN}}(z)/\sigma_8(z)$, are based on the best power law fit parameter and from HOD modeling (HOD). To derive $\log M_{\text{DMH}}^{\text{typ}}$, we use the bias parameter from HOD modeling. See Table 1 for the definition of the samples.

sample is $(9.77 \pm 0.16) \times 10^{-4} h^3 \text{ Mpc}^{-3}$. We use the five-parameter model by Zheng et al. (2007) to represent the central and satellite HODs of our low redshift tracer set:

$$\langle N_{G,c} \rangle(M_h) = \frac{1}{2} \left[1 + \text{erf} \left(\frac{\log M_h - \log M_{\min}}{\sigma_{\log M}} \right) \right]$$

$$\langle N_{G,s} \rangle(M_h) = \langle N_{G,c} \rangle(M_h) \left(\frac{M_h - M_0}{M'_1} \right)^{\alpha_s}. \quad (8)$$

This form involves a step function with a lower mass

cutoff M_{\min} , which is smoothed by incorporating the error function (erf) with the width of the cutoff profile $\sigma_{\log M}$. For the detailed description of the different parameters, see Sect. 3.2 of Zheng et al. (2007). A limitation of our current fitting software is that it allows a maximum of two simultaneous variable parameters. Thus, we search for acceptable fits in a two parameter space, while fixing other parameters to reasonable values. We note that, for our current purposes in this paper of obtaining correct b_A values, which is mainly constrained by the two halo term, the detail of the HOD is not critical (see dis-

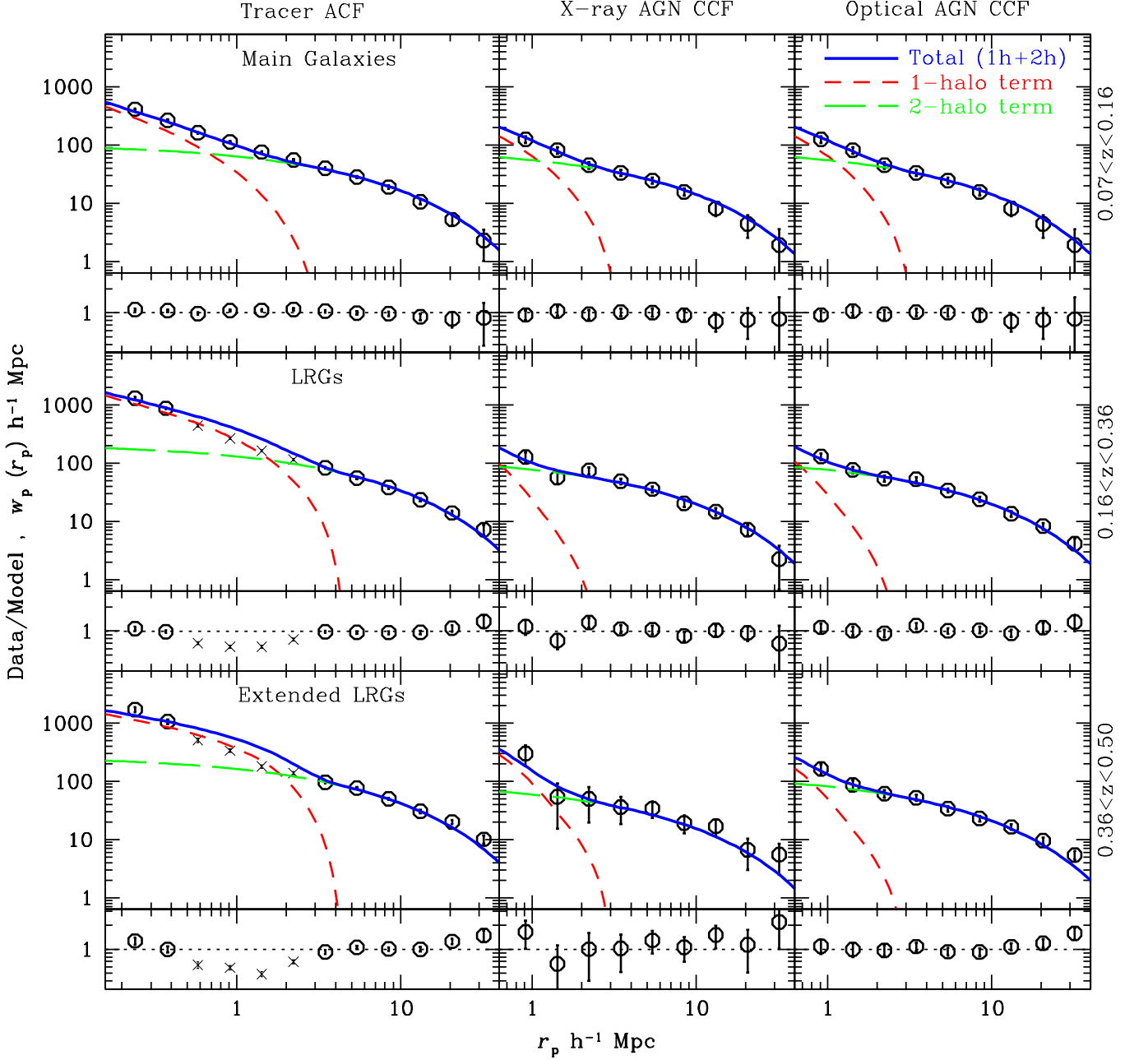


FIG. 8.— Projected tracer set ACFs and CCFs between the different total AGN samples and tracer sets in the corresponding redshift ranges. The order of the panels is the same as in Fig. 7. Each ACF/CCF plot contains the corresponding best-fit HOD model (blue solid line) along with the one halo (red dashed line) and two halo (green long-dashed line) terms and shows the residuals (data/model) below each individual plot. We show the r_p range that is used for the fits, i.e., $r_p > 0.2 h^{-1}$ Mpc and $r_p > 0.7 h^{-1}$ Mpc for the tracer ACFs and the AGN-tracer CCFs respectively. The LRG ACF data points shown as crosses are not used in the fit (see Sect. 5.1.2).

cussions below in Sect. 5.2). A Code that searches for the best-fit values and confidence ranges of model parameters in a many-parameter space using the Markov-Chain Monte-Carlo (MCMC) is under development and will be used in a future paper.

Zheng et al. (2007) perform fits to the full five parameter space for several luminosity-threshold subsets of the SDSS main galaxy sample. We take advantage of the results of their $M_r < 21.0$ sample, which has a similar selection criteria to our SDSS main galaxy sample, and use their results to fix three parameters: $\log(M_0/[h^{-1} M_\odot]) = 11.92$, $\log(M'_1/[h^{-1} M_\odot]) = 13.94$,

and $\sigma_{\log M} = 0.39$. We then search for the best fit model for our measurement of the SDSS main galaxy ACF in the remaining two parameters ($\log M_{\min}$ and α_s) by minimizing the correlated χ^2 , taking into account the density constraint (see Eq. 18 of paper II). We find an excellent fit to the data with the best fit values and 1σ uncertainties of $\log(M_{\min}/[h^{-1} M_\odot]) = 12.81 \pm 0.01$ and $\alpha_s = 1.16 \pm 0.02$, with an associated bias parameter of $b_G = 1.43 \pm 0.01$. The uncertainties in these values are lower than those in Zheng et al. (2007) as we perform the fit with only two free parameters instead of five. For the fit, we use $w_p(r_p)$ measurements in the range $0.2 < r_p[h^{-1} \text{Mpc}] < 40$.

First, we follow our HOD modeling described in paper II and exclude data points that fall in the transition region between the one halo dominated and two halo dominated regimes. In the case of the SDSS main galaxy sample, using scales of $0.4 < r_p [h^{-1} \text{ Mpc}] < 1$ results in essentially the identical best-fit HOD. The SDSS main galaxy ACF and the best fit model are shown in Fig. 8 (upper left panel).

5.1.2. Luminous Red Galaxies ($0.16 < z < 0.36$)

The tracer set in the intermediate redshift range is the LRG sample with $-23.2 < M_g^{0.3} < -21.2$ (Sect. 2.2). The derivation of central and satellite HODs of this sample is described in detail in paper II. In summary, we start from the results of Zheng et al. (2009) and make a two parameter adjustment to find the HOD that fits best to our LRG ACF, including the number density constraint. For satellite LRGs, we interpolate between the $\Delta\chi^2 = 4$ upper and lower bounds of the satellite HOD by Zheng et al. (2009), while for the central LRG HOD we shift their central HOD horizontally along the $\log M_h$ axis. First, we fit $w_p(r_p)$ measurements in the $0.2 < r_p [h^{-1} \text{ Mpc}] < 40$ range. Significant residuals remain in the transition region between the one halo and two halo term dominated regimes, due to the fact that our HOD modeling neglect the effects of halo-halo collisions in the two halo term. Unlike with the main galaxy sample, this effect is not negligible with the LRG sample, due to a larger transition region. We therefore neglect data points in a range of $0.46 < r_p [h^{-1} \text{ Mpc}] < 2.8$ and find a good fit to the data (Fig. 8, middle left panel). The associated LRG bias parameter is $b_G = 2.20 \pm 0.01$, where this error includes only the statistical 1σ uncertainty of the fit.

5.1.3. Extended LRGs ($0.36 < z < 0.50$)

Unlike for the cases of the SDSS main galaxy and LRG samples, there is no template HOD model in the literature for a sample with almost identical selection criteria to those for our extended LRG sample, i.e., a non-volume limited sample of LRGs with $-23.2 < M_g^{0.3} < -21.7$ at $0.36 < z < 0.50$.

The closest sample that we can use as our template is the $-23.2 < M_g^{0.3} < -21.8$, $z \sim 0.3$ LRG sample, for which Zheng et al. (2009) made a detailed HOD investigation, in addition to the $-23.2 < M_g^{0.3} < -21.2$ LRG sample. Thus, we follow the approach in paper II for the LRG sample and search for the best-fit HOD model of the ACF of our extended LRG sample by adjusting Zheng et al. (2009) HOD results for the $-23.2 < M_g^{0.3} < -21.8$ LRG sample.

In short, we take the central and satellite HODs from Fig. 1 (b) of Zheng et al. (2009) and search for the best-fit HOD by tweaking the template. We shift their central HOD horizontally by d in $\log M_h$ and interpolate between their upper and lower bounds ($\Delta\chi^2$) of their satellite HOD, with the dividing ratio of $f : (1 - f)$, where $f = 0$ ($f = 1$) represents their lower (upper) bound on the satellite HOD (see paper II for details). We search for the best-fit HOD model in the (f, d) space, where the HOD-model predicted $w_p(r_p)$ function is calculated at $z = 0.42$. As with the LRGs, we exclude the $0.46 < r_p [h^{-1} \text{ Mpc}] < 2.8$ range from the fit. We obtain

the best-fit with $f = 4.2 \pm 0.8$ and $d = -0.29 \pm 0.04$. We do not use the density constraint in the fit, because the extended LRG sample is not volume-limited and therefore the number density is not accurately determined. However, the best-fit model gives a density of $4.3 \times 10^{-5} h^3 \text{ Mpc}^{-3}$, which is close to the number density of the extended LRGs calculated in the volume-limited portion of the sample (see Table 1).

5.2. AGN biases and Typical Halo Masses

For the AGN HOD model, we use model B of paper II, which parameterizes the number of central ($\langle N_{A,c} \rangle$) and satellite ($\langle N_{A,s} \rangle$) AGNs in a DMH:

$$\begin{aligned} \langle N_{A,c} \rangle &= f_A \Theta(M_h - M_{\min}), \\ \langle N_{A,s} \rangle &= f_A \Theta(M_h - M_{\min}) (M_h/M_1)^{\alpha_s}, \end{aligned} \quad (9)$$

where $\Theta(x)$ is the step function (equal to 1 at $x \geq 0$; 0 at $x < 0$) and f_A represents the AGN fraction (duty cycle) among central galaxies at $M_h \gtrsim M_{\min}$. We use $\log M_1/M_{\min} = 1.36$ in Eq. 9, which Zehavi et al. (2005b) find to be a typical value at which a DMH hosts on average one satellite galaxy in addition to a central galaxy. We model the CCFs between our tracer sets and the AGNs using the same method as in paper II:

$$\begin{aligned} P_{AG,1h}(k) &= \frac{1}{(2\pi)^3 n_A n_G} \int \phi(M_h) \times \\ &\quad [\langle N_{A,c} N_{G,s} + N_{A,s} N_{G,c} \rangle(M_h) y(k, M_h) + \\ &\quad \langle N_{A,s} N_{G,s} \rangle(M_h) |y(k, M_h)|^2] dM_h, \end{aligned} \quad (10)$$

$$P_{AG,2h}(k) \approx b_A b_G P_{lin}(k), \quad (11)$$

and

$$w_p(r_p) = \int \frac{k}{2\pi} [P_{1h}(k) + P_{2h}(k)] J_0(kr_p) dk \quad (12)$$

where $n_A(n_G)$ is the number density of AGNs (tracers), $y(k, M_h)$ is the Fourier transform of the Navarro, Frenk, & White profile (NFW; Navarro et al. 1997), $P_{lin}(k)$ is the linear power spectrum of the density field with the transfer function by Eisenstein & Hu (1998), and $J_0(x)$ is the zeroth-order Bessel function of the first kind.

Due to the low space density of AGNs, most CCFs do not have a signal-to-noise ratio on small scales that is sufficient for applying the χ^2 statistics. While a majority of CCFs contain $\gtrsim 16$ pairs per bin at $r_p > 0.3 h^{-1} \text{ Mpc}$, we have to exclude $r_p < 0.7 h^{-1} \text{ Mpc}$ bins for several CCFs in order to have at least 16 AGN-galaxy pairs per bin. To derive b_A in a consistent way for all CCFs, we use only $r_p > 0.7 h^{-1} \text{ Mpc}$ bins to derive column ‘ $b(z)$ HOD’ for all of the AGN samples given in Table 3.

Since the purpose of using the HOD modeling in this paper is to derive reliable values of b_A , we do not discuss detailed results using other models, which will be presented in Miyaji et al. (in preparation). The derived bias parameter, which is mainly constrained by the two halo term, is not very sensitive to our particular choice of HOD model. To verify this, we repeat the HOD fits to the CCFs with different values of the parameter $\log M_1/M_{\min}$ (Eq. 9). For various SDSS luminosity-threshold galaxy samples, Zehavi et al. (2005b) found the range of this parameter to be $1.0 \lesssim \log M_1/M_{\min} \lesssim$

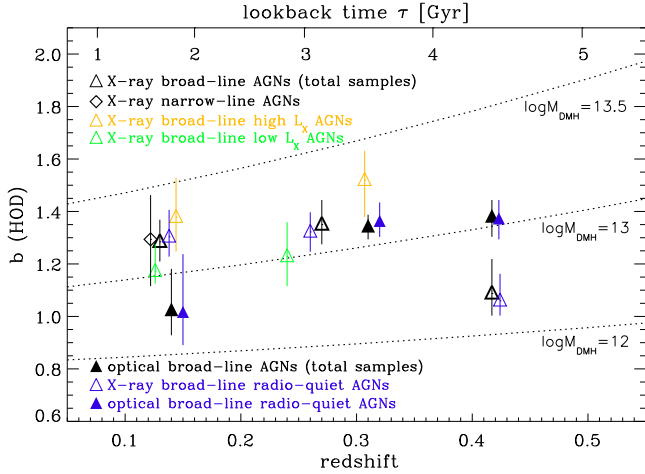


FIG. 9.— HOD modeling bias parameter b_{AGN} as a function of redshift for our X-ray selected RASS/SDSS samples (open symbols) and optically-selected SDSS AGN samples (filled symbols). Black symbols represent the total AGN samples, while colored symbols represent subsamples (low and high L_X in green and yellow, radio-quiet in blue). The dotted lines show the expected $b(z)$ of typical DMH masses M_{DMH} based on Sheth et al. (2001) and Tinker et al. (2005), where masses are given in $\log M_{\text{DMH}}$ in units of $h^{-1} M_{\odot}$. For visualization purposes, we slightly shift the redshifts of some AGN samples.

1.5. Thus we fix $\log M_1/M_{\text{min}}$ to 1.0, 1.36 (our default), and 1.6 and obtain b_A values in each case. The best fit values of b_A typically vary only by ≈ 0.01 among these three cases, demonstrating the robustness of deriving the bias parameter using this method.

5.3. AGN HOD bias results

In Fig. 9 we present the main results of our study. We show the HOD bias parameter for our different X-ray and optically-selected AGN samples as a function of redshift. All AGN samples are consistent with a host DMH mass of $\log (M_{\text{DMH}}/[h^{-1} M_{\odot}]) \sim 12.4 - 13.4$ (see Table 3). Samples in which the radio-loud AGNs have been excluded have very similar clustering amplitudes as the total samples, in all three redshift ranges. The clustering signal of narrow-line RASS/SDSS AGNs at $0.07 < z < 0.16$ is also very similar to broad-line RASS/SDSS AGNs at the same redshift. Furthermore, weak X-ray luminosity dependences on the broad-line AGN clustering amplitude are found at both $0.07 < z < 0.16$ and $0.16 < z < 0.36$.

5.4. Power Law versus HOD Derived Bias Parameters

The various AGN samples studied here allow us to compare the power law fit derived bias parameters with those from HOD modeling. In Fig. 10 we plot the bias values from the power law fits and HOD modeling listed in Table 3. The $b(\text{HOD})$ values are often larger than the $b(\text{power law fit})$ values. Furthermore, the uncertainties on the HOD bias are often lower than on the power law bias. This is because the power law fits are based on the inferred ACF, while the HOD modeling is directly applied to the CCF which has lower statistical uncertainties.

The relatively narrower distribution and on-average higher $b(\text{HOD})$ values compared to the $b(\text{power law fit})$ values are caused by strong variations between the samples in the one halo term, while the variations in the two halo term are smaller. As described in the beginning of

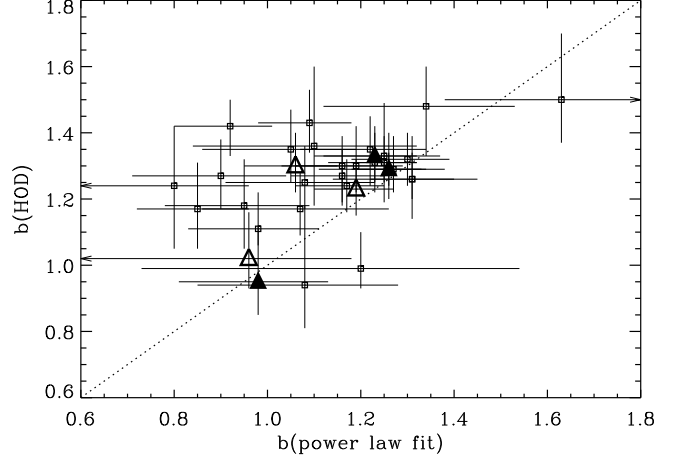


FIG. 10.— Comparison between bias parameters derived from power law fit versus HOD modeling. We highlight the most important samples at the three redshift ranges: total X-ray selected RASS/SDSS AGN samples (open triangles) and total optically selected SDSS AGN samples (filled triangles). The 1σ uncertainties for the different methods are plotted as error bars. The dotted line shows a 1:1 correspondence.

Section 5, power law fit bias measurements commonly use smaller scales that are in the one halo term (our fitted range is $r_p = 0.3 - 15 h^{-1} \text{ Mpc}$) in order to increase the statistical significance. If power law fits are restricted only to larger scales, the method suffers from the problem that the lowest scale where the linear biasing scheme can still be applied varies from sample to sample and remains ambiguous. HOD modeling allows, in principle, the use of the full range of scales since the method first determines the one and two halo terms and then constrains the linear using data down to the smallest r_p values that are dominated by the two halo term for each individual sample.

Therefore, an apparently low power law bias value of one sample compared to another can be due to a lower clustering strength in the one halo term, while the “true” linear bias parameters may be similar. If we use scales of $r_p > 1.5 h^{-1} \text{ Mpc}$ for the power law fits, the errors on the bias are much larger, but the values are statistically consistent with those derived from the HOD model fits.

In summary, on small ($\lesssim 1 h^{-1} \text{ Mpc}$) and large ($\gtrsim 10 h^{-1} \text{ Mpc}$) scales a power law model is not a good fit to the data. HOD modeling is currently the optimal method to establish the large-scale bias parameter, provided the adopted HOD parameterization can adequately describe the true galaxy and AGN DMH population. With larger data sets in the future, the uncertainties in the measurements will be decreased further. To derive a reliable picture of AGN clustering, bias parameters should be inferred from HOD modeling, or at least from the comparison of the correlation function with that of the dark matter only in the linear regime (Allevato et al. 2011), because systematic errors based on power law bias parameters will be larger than the statistical uncertainties of the clustering measurement. In the following discussions, we use the HOD model bias parameters whenever we compare our different AGN samples. In the case where we compare our results to other studies, which list only power law fit bias values, we also use power law fit bias values to be consistent.

6. DISCUSSION

Our clustering measurements of luminous broad-line AGNs yield three independent data points in the poorly-studied low-redshift range for both X-ray and optically-selected broad-line AGNs. In addition, we measure the clustering signal of X-ray detected narrow-line AGNs. We derive the bias parameter of the different samples based on power law fits and HOD modeling.

6.1. Comparison with X-ray selected broad-line AGN Clustering Measurements

There are no published clustering measurements of X-ray selected broad-line AGNs with comparable low uncertainties at low redshifts. For example, Mullis et al. (2004) measure the clustering strength of broad-line AGNs in the *ROSAT* NEP survey, for which we derive a bias parameter of $b = 1.83^{+1.88}_{-0.61}$ ($z = 0.22$, paper I).

At higher redshift Allevato et al. (2011) compute the clustering strength of X-ray (0.5–2 keV) unabsorbed & absorbed and narrow & broad-line AGN in the *XMM-Newton* COSMOS field in different bins where the median redshift of the subsamples varies from $z = 0.5$ to $z = 2.5$. They find that broad-line AGNs reside in DMH of $\log(M_{\text{DMH}}/[h^{-1}M_{\odot}]) \sim 13.2$, independent of redshift. The average luminosity of their broad-line AGN sample is $\log(L_{2-10\text{ keV}}/[\text{ergs}^{-1}]) \sim 44.1$ (intrinsic absorption-corrected luminosity; V. Allevato, private communication 2011) which corresponds to $\log(L_{0.1-2.4\text{ keV}}/[\text{ergs}^{-1}]) \sim 44.2$ assuming $\Gamma = 1.8$. Consequently, the broad-line AGNs studied by Allevato et al. (2011) have X-ray luminosities comparable to our total RASS/SDSS AGN sample at $0.16 < z < 0.36$. The derived DMH mass of $\log(M_{\text{DMH}}/[h^{-1}M_{\odot}]) \sim 13.2$ for our low-redshift RASS/SDSS AGN sample is in excellent agreement with the value found at $z \sim 1.5$ for the broad-line AGN sample of Allevato et al. (2011).

6.2. Optical versus X-ray selected AGN clustering properties

Our study allows us to compare X-ray and optically-selected AGN clustering measurements over three independent low redshift ranges. As the same procedure and identical tracer sets are used for calculating the clustering strengths of the X-ray and optically-selected AGN samples, we expect there to be minimal systematic errors when comparing the clustering properties among our different AGN samples.

Since most of the results in the literature are based on power law fits to the correlation function, we compare our power law bias parameters from various clustering measurements of X-ray and optically-selected SDSS AGN samples and galaxy clustering measurements in Fig. 11. The bias values of our X-ray and optically-selected AGN populations clearly fall within the region occupied by $\sim L^*$ galaxies.

We do not find a very significant difference between the clustering amplitude of our broad-line optical and X-ray AGN samples in the different redshift ranges considered here. The differences in the HOD model bias parameters between the total X-ray and optically-selected AGN samples in our three (increasing) redshift ranges are 1.5σ , 0.1σ , and 2.0σ . As our samples at $0.16 < z < 0.36$ have many more X-ray and optically-selected AGNs than the

samples at lower and higher redshifts, we consider the results in this redshift range to be the most reliable. We do not find a significant difference in the clustering of X-ray and optically-selected AGN in this redshift range. Moreover, given that only one out of three sample has a difference of $\sim 2.0\sigma$, we conclude that it is likely not significant.

Although the RASS/SDSS AGN samples extend to lower AGN luminosities than the optically-selected SDSS AGNs, both samples span roughly the same luminosity range for broad-line AGNs, which may account for the similar clustering properties. RASS and SDSS are also well matched in terms of the depth and selection of broad-line AGNs (see Anderson et al. 2003, 2007). Optical surveys are known to find at brighter magnitudes predominantly X-ray unabsorbed broad-emission line AGNs. *ROSAT*'s soft energy range allows primarily for the detection of X-ray unabsorbed AGN and, hence, is also biased also toward broad-line AGNs. Therefore, we do not expect strong systematic differences between these samples due to the RASS/SDSS AGN selection.

For the optically-selected SDSS broad-line AGNs in the redshift ranges of $0.16 < z < 0.36$ and $0.36 < z < 0.50$, the sample is large enough to create subsamples of optically-selected AGN that are not detected in RASS. Furthermore, at $0.16 < z < 0.36$ we select optically-selected AGNs that are also detected by RASS. We use these samples as a consistency check to verify that the clustering properties between X-ray and optically-selected AGN samples are not significantly different. As shown in Table 3 all of these AGN samples agree well within their 1σ uncertainties in their HOD model bias parameters. This provides compelling evidence that there is indeed no strong difference between broad-line X-ray and optically-selected AGNs at similar luminosities at low redshifts.

Figure 11 compares our AGN clustering results to other X-ray and optically-selected AGN clustering studies. The properties of various clustering studies are given in Table 4 of paper I. Hickox et al. (2009) study the clustering properties of AGNs in the AGES survey. As they publish only the AGN CCFs with galaxies, we use their best power law fits (R. Hickox, private communication 2011) to infer their AGN ACF and the bias parameter, following our approach described in Sect. 4.1. From the redshift distributions presented in Hickox et al. (2009), we compute the effective median redshift for the CCFs ($\bar{z}_{\text{eff}} = 0.37$) and derive a bias value of $b_{\text{X,H09}} = 1.20^{+0.09}_{-0.09}$.

Our finding of detecting no significant difference in the AGN clustering properties between X-ray and optically-selected AGNs at low redshifts may appear to be in contrast to AGN clustering measurements at higher redshifts ($z > 0.7$), where optically-selected AGN samples have a lower clustering strength than X-ray selected AGN samples (Fig. 11). Furthermore, the clustering of X-ray selected AGNs is roughly consistent with red galaxies at higher redshifts. However, some of the X-ray clustering studies significantly underestimate their uncertainties by using Poisson errors instead of jackknife errors. Moreover, X-ray and optically-selected AGN samples at these redshifts select AGNs with different intrinsic properties. While the optical AGNs are mainly drawn from large sky

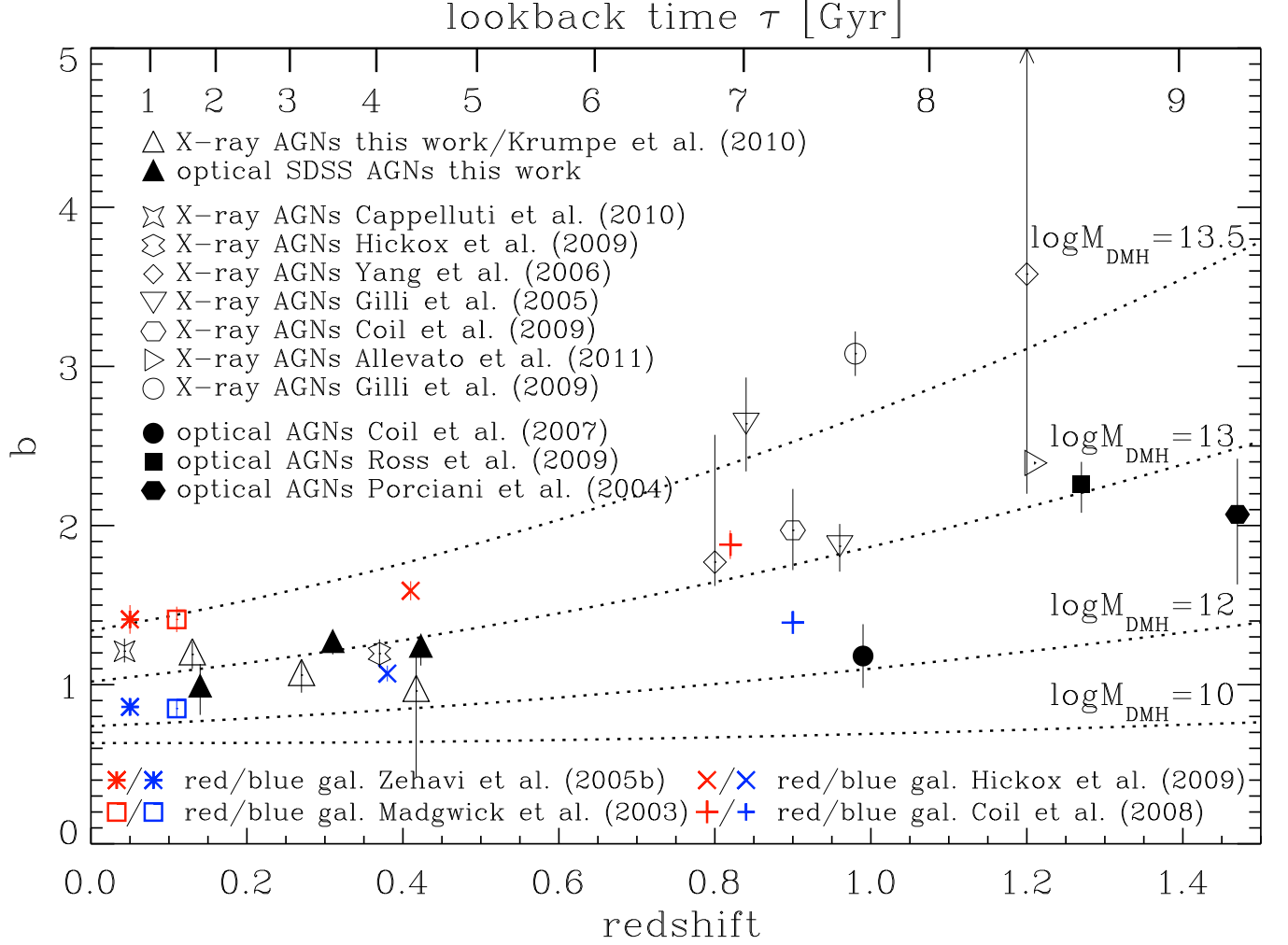


FIG. 11.— Power law bias parameter $b_{\text{AGN}} = \sigma_{8,\text{AGN}}(z)/\sigma_8 D(z)$ as a function of redshift for various X-ray and optically-selected AGN samples as well as blue and red galaxies. We plot our power law fit bias parameters to compare different studies in a consistent manner. Black open symbols represent X-ray selected AGN samples, while black filled symbols represent optically-selected AGN samples. Clustering measurements for red and blue galaxies are shown as red and blue symbols at different redshifts. For the explanation of the dotted lines see Fig. 9. For visualization purposes, we slightly offset the redshifts of the X-ray and optically-selected SDSS AGN samples.

area surveys and sample luminous predominantly broad-line AGNs, the X-ray selected AGN samples derive from very deep observations covering only a few square degrees on the sky. Consequently, the X-ray selected AGNs have, on average, much lower luminosities. Additionally, the X-ray samples include absorbed AGNs, which results in a large fraction of narrow-line AGNs that are missed in the optical AGN samples at these redshifts.

6.3. Broad-line versus Narrow-line AGNs

The differences in the clustering signals between X-ray and optically-selected AGN samples at $z > 0.7$ can potentially be accounted for either as the result of a large luminosity difference between the samples or the large fraction of X-ray absorbed, optically narrow-line AGNs in the X-ray AGN samples.

To test the latter assumption, we measure the clustering properties of narrow-line RASS/SDSS AGNs classified by Anderson et al. (2007) in the redshift ranges of $0.07 < z < 0.16$ and $0.16 < z < 0.36$. The low number density of narrow-line RASS/SDSS AGNs at $0.16 < z < 0.36$ forces us to use scales of $r_P > 1.1 h^{-1}$ Mpc to

apply the χ^2 -statistics during the HOD modeling. The clustering strength of the narrow-line and total broad-line RASS/SDSS AGN samples at $0.07 < z < 0.16$ agree well with each other (Table 3), although the uncertainty for the narrow-line AGN sample is large. The power law fit bias parameter for the narrow-line RASS/SDSS AGN sample is significantly lower than the bias derived from the HOD model (see Fig. 9) and would suggest a significantly lower clustering amplitude than the broad-line RASS/SDSS AGN sample. This is caused by differences between the samples on small scales where the one halo term dominates. The power law fits use these small scales, while the HOD modeling mainly relies on the two halo term to determine the large-scale clustering.

At $0.16 < z < 0.36$ the narrow-line AGN HOD bias parameter is too poorly constrained ($b = 1.01^{+0.24}_{-0.17}$) to allow for a detailed interpretation. While we cannot determine whether narrow-line RASS/SDSS AGNs cluster similarly or less than broad-line AGNs in that redshift range, we can rule out the conclusion that they are significantly more clustered. Two important points are worth noting: first, as *ROSAT* can detect only

moderately X-ray absorbed AGNs ($\log(N_{\text{H}}/[\text{cm}^{-2}]) \lesssim 22$), while *XMM-Newton* and *Chandra* are sensitive to much more absorbed (and lower luminosity) AGNs, the narrow-line AGNs detected by RASS may not be as common. Second, the relative clustering strength of narrow-line AGNs could change with redshift if there is a difference in how AGN activity is triggered at different cosmological epochs. However, other studies confirm that low-redshift narrow-line (radio-quiet) AGNs are not strongly clustered and are hosted in galaxies that do not differ significantly from typical non-AGN galaxies (e.g., Mandelbaum et al. 2009, Li et al. 2006).

Allevato et al. (2011) find that X-ray selected narrow-line AGNs in the *XMM-Newton* COSMOS field cluster slightly lower (2.3σ) than X-ray selected broad-line AGNs and reside in DMHs of $\log(M_{\text{DMH}}/[h^{-1} M_{\odot}]) \sim 13.0$ in the redshift range $z \sim 0.5 - 1.0$. However, their narrow-line AGNs have an average intrinsic (absorption corrected) $\log(L_{2-10 \text{ keV}}/[\text{ergs}^{-1}]) = 43.1$ (V. Allevato, private communication 2011) which is an order of magnitude lower than the average luminosity of their broad-line AGNs. When Allevato et al. (2011) consider only the X-ray properties of the sources to create X-ray absorbed and X-ray unabsorbed subsamples, in which both have an almost identical mean luminosity of $\log(L_{2-10 \text{ keV}}/[\text{ergs}^{-1}]) \sim 43.65$, they find that X-ray absorbed AGNs cluster slightly less (2.6σ) than X-ray unabsorbed AGNs.

To summarize, the difference between the AGN clustering properties between X-ray and optically-selected AGN samples at $z > 0.7$ is likely not due to a strongly clustered population of narrow-line AGNs in the X-ray samples. However, these objects do have significantly lower luminosities than optically-selected broad-line AGNs.

6.4. Impact of Radio-loud Broad-line AGN on the Clustering Signal

For each of the various broad-line AGN samples studied here, we create subsamples where we have excluded radio-detected AGNs to study the impact of radio-loud AGNs on the derived clustering strength. We do not find any significant differences between the AGN samples that include or exclude radio-detected AGNs. The HOD bias parameters for these samples agree well within their 1σ uncertainties in all three redshift ranges studied (see Fig. 9). However, the samples are similar as only approximately 10–20% of all broad-line AGNs have also radio (FIRST) detections, so this result may not be particularly constraining.

As mentioned in Section 3.2, the SDSS AGN target selection gives the highest priority to point sources that are detected in FIRST (above a certain flux limit) without considering their colors. We select all AGNs ($n = 187$) with $0.16 < z < 0.36$ which have the SDSS FIRST target selection flag equal to 1. Hence, these objects were only selected on the basis of having a significant FIRST radio flux and can be understood as a well-defined radio-selected AGN sample ($\langle z \rangle = 0.28$, $\langle M_i \rangle = -23.28$). We compute the CCF of this AGN sample with the LRG tracer set. Due to the low number of AGNs in this sample, the HOD bias parameter has large uncertainties, with a value of $b = 1.45^{+0.24}_{-0.29}$. A sample of all 423 SDSS AGNs that have a radio-detection (including the

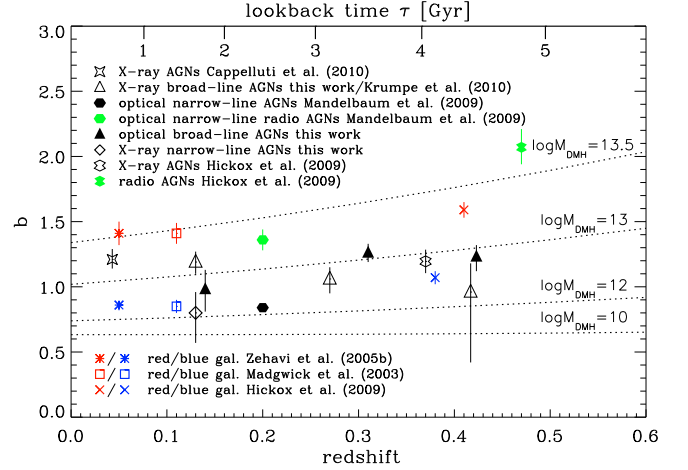


FIG. 12.— Power law bias versus redshift (similar to Fig. 9), comparing the clustering of differently-selected AGN samples (radio and non-radio samples) and galaxies. Note that the HOD model bias parameter for the narrow-line RASS/SDSS AGN sample is significant higher ($b = 1.24^{+0.18}_{-0.19}$) than the power law bias shown here.

187 radio-selected SDSS AGNs; $\langle z \rangle = 0.27$, $\langle M_i \rangle = -22.84$) yields $b = 0.97^{+0.18}_{-0.19}$. Furthermore, we compute the CCF of only the RASS/SDSS AGNs with $0.16 < z < 0.36$ that are marked as radio sources in Anderson et al. (2007). The sample, which contains 144 objects and has $\langle z \rangle = 0.25$ and $\log(L_{0.1-2.4 \text{ keV}}/[\text{ergs}^{-1}]) \sim 44.36$, yields a HOD bias parameter of $b = 1.08^{+0.30}_{-0.32}$. No constraining results can be drawn by using only radio-detected SDSS AGN samples, because these samples contain too few objects. However, all values are consistent with the clustering strengths of the other AGN samples in the same redshift range.

Many previous studies (e.g., Magliocchetti et al. 2004; Hickox et al. 2009; Mandelbaum et al. 2009) found that radio-loud AGNs cluster more strongly than AGNs without the presence of radio emission. At first glance our results may appear to be in contrast to these findings. However, those studies focus on the clustering properties of optical narrow-line (instead of broad-line) AGNs based on diagnostic emission-line ratios and radio luminosity. Moreover, when comparing the clustering strength of different samples it is essential to take into account the involved luminosities. Figure 12 shows the bias of various AGN and galaxy samples at lower redshift ($z \leq 0.6$), focusing on comparing radio-selected AGN samples. For the radio (non-broad-line) AGN sample of Hickox et al. (2009), we derive a bias value of $b_{\text{radio, Hi09}} = 2.07^{+0.14}_{-0.13}$ ($\bar{z}_{\text{eff}} = 0.47$) by following the description given in Sect. 6.2.

Magliocchetti et al. (2004) find that radio (FIRST) galaxies with AGN activity cluster more strongly than both radio-detected 2dFGRS galaxies without AGN activity and 2dFGRS galaxies without radio emission. It is not clear, however, whether the different galaxy samples have similar luminosities and colors. If the galaxy samples that are used for comparison are mainly blue, star-forming galaxies, one would expect a significant difference in the clustering strength based on the different host galaxy properties. Consequently, the clustering difference could reflect not by AGN activity but host galaxy

type. The high bias parameter for radio-loud AGNs ($b = 2.07^{+0.14}_{-0.13}$) and moderate bias ($b = 1.20^{+0.09}_{-0.09}$) for X-ray selected AGNs in Hickox et al. (2009) can also be explained by the different host galaxy populations (see their Fig. 9).

Mandelbaum et al. (2009) compare the clustering strength of optically-selected narrow-line AGNs ($0.01 < z < 0.3$ and $-23 < M_r^{0.1} < -17$) with and without radio emission at *fixed* stellar mass, i.e., at fixed luminosity and color. They find that at fixed stellar mass radio-loud narrow-line AGNs cluster more strongly and hence reside in more massive DMHs than narrow-line AGNs without radio emission and galaxies without the presence of AGN activity (see Fig. 12). Neither Magliocchetti et al. (2004) nor Mandelbaum et al. (2009) detect a difference in the clustering properties within the radio-loud narrow-line AGN sample as a function of radio luminosity.

Shen et al. (2009) compute the ACF of optical SDSS DR5 AGNs (from the Schneider et al. 2007 sample) in the redshift range $0.4 \lesssim z \lesssim 2.5$. As we do here, they divide their samples into FIRST-detected and undetected sources. Their fits (over the range $3\text{--}115 h^{-1}$ Mpc) suffer large uncertainties; therefore, they fix the slope of the power law fit for all samples to $\gamma = 2$. They compute the ACF of the FIRST-undetected SDSS AGNs. When they compare this result to the CCF between FIRST-detected and undetected SDSS AGNs, they find a 2.5σ difference in r_0 , using only the diagonal elements of the covariance matrix. Fixing the slope and not using the full covariance matrix likely increases the systematic uncertainties in their results. By contrast, our measurements test a much narrower redshift range, use the full covariance matrix, allow free r_0 and γ values for the power law fits, and use the HOD modeling approach. Shen et al. (2009) test much brighter AGN samples at higher redshifts than our samples here. The fact that they find a difference in the clustering of radio-detected versus non-detected AGNs and we do not may be a consequence of the samples having different luminosities or redshifts.

If broad-line AGNs at $z < 0.5$ indeed have no clustering dependence on radio emission, this may suggest that different physical mechanisms trigger radio emission in broad-line and narrow-line AGNs, as narrow-line AGNs do have a clustering dependence with radio emission (Mandelbaum et al. 2009) at fixed stellar mass. This would be somewhat surprising as significant radio emission in all AGNs is believed to be related to jet phenomena (e.g., Blandford & Payne 1982).

6.5. Luminosity Dependence of the Clustering Signal

In papers I and II, we reported a possible X-ray luminosity-dependence in the AGN clustering strength of RASS/SDSS AGN in the redshift range $0.16 < z < 0.36$ (see also Fig. 9, green and yellow green symbols). The exclusion of radio-detected RASS/SDSS AGNs performed here tests whether the weak L_X -dependence of AGN clustering observed is due to the presence of radio-loud AGNs in the higher L_X sample (see Sect. 3.1.1).

As shown in paper II, this luminosity-dependent clustering is more significant in the one halo term than in the two halo term. Using only larger scales of $r_P > 0.7 h^{-1}$ Mpc for the HOD modeling in this paper (in order to derive bias parameter in a consistent way for all AGN

samples) increases the error on the individual measurements. This results in a decrease in the significance of the luminosity-dependent clustering. We find that the 1.5σ (2.0σ using the power law bias of this paper) clustering difference between the lower and higher L_X AGN samples remains roughly constant when we exclude radio-detect AGNs from both subsamples (1.7σ using the HOD bias; 2.4σ using the power law bias of this paper).

The difference in the clustering strength of the lower and higher L_X RASS/SDSS AGN samples in the redshift range of $0.07 < z < 0.16$ is 1.2σ (HOD model). The error bars on the bias of these samples are high, due to the low number of objects. The significance of the individual redshift measurements do not provide strong evidence for an X-ray luminosity dependence of the AGN clustering strength.

Other studies find similar weak trends at low redshifts (Fig. 12). Cappelluti et al. (2010) compute the clustering signal for *Swift*/BAT 15–55 keV selected AGNs and find a clustering difference of 1.6σ for the higher L_X AGNs relative to the lower L_X AGNs. Comparing the photometric galaxy density around spectroscopic SDSS AGNs, Serber et al. (2006) and Strand et al. (2008) find that higher luminosity AGNs have more overdense galaxy environments compared to lower luminosity AGNs at scales smaller than 0.5 Mpc. These studies are not directly measuring AGN clustering, rather they focus on the immediate environments of AGNs.

We do not detect an optical luminosity-dependence of the RASS/SDSS AGN clustering. Given the large sample size and low resulting errors in these samples, this is a constraining result. Previous clustering measurements of optically-selected AGNs using the 2dF QSO Redshift Survey (2QZ, Boyle et al. 2000), 2dF-SDSS LRG and QSO (2SLAQ, Cannon et al. 2006), and SDSS also find little evidence for an optical luminosity dependence of the AGN clustering strength (e.g., Croom et al. 2002; da Ângela et al. 2008; Mountrichas et al. 2009). Mountrichas et al. (2009) use CCFs between AGNs and LRGs and find some indication that bright SDSS AGNs cluster less than faint 2SLAQ QSOs, although the result is only marginally significant (1.6σ). On the other hand, Shen et al. (2009) detect a stronger clustering strength for the 10% most luminous SDSS DR5 AGNs ($0.4 \lesssim z \lesssim 2.5$) at the $\sim 2\sigma$ level. However, they caution that the dynamical range in luminosity probed is narrow and the sample size in the luminosity subsamples not large enough to yield constraining clustering measurements. Porciani & Norberg (2006) suggest that a luminosity dependence of the clustering may be more evident at $z > 1.3$, while da Ângela et al. (2008) find hints that the lower redshift ranges ($z < 1.3$) may show more dependence with luminosity.

The optical and X-ray luminosities of broad-line AGNs are connected via the optical-to-X-ray spectral index, which measures the ratio of the rest-frame luminosity density at 2500 Å to 2 keV. Although the relation has some scatter (see Anderson et al. 2007 for the optical-to-X-ray spectral index for RASS/SDSS AGNs), more X-ray luminous AGNs are, on average, also intrinsically brighter in the optical. If indeed there is a weak X-ray luminosity dependence of the AGN clustering strength, the very narrow M_i range that the optical SDSS AGNs span

would hamper a detection. Identifying AGN activity using X-ray emission allows us to identify low-luminosity AGNs, where the optical light is dominated by the host galaxy. This results in a wider luminosity range in X-ray emission than in the optical (Fig. 6, lower panel) in the two lowest redshift ranges. At $0.16 < z < 0.36$, the mean optical luminosity of the high M_i SDSS AGN sample is only a factor 2 higher (0.75 mag) than the low M_i SDSS AGN sample, while the X-ray luminosities between the high and low L_X samples differ by a factor of 4.4. This is also seen when considering the luminosity difference between the 90th percentile in the high luminosity samples and the 10th percentile in the low luminosity samples (factor $f = 4.3$ for optical SDSS AGNs, $f = 17.8$ for RASS/SDSS AGNs) and covered luminosity range ($f = 30$ for optical SDSS AGNs, $f = 310$ for RASS/SDSS AGNs).

Hence, to detect a possible optical luminosity dependence in the broad-line AGN clustering strength, as might be expected if there is a weak X-ray luminosity dependence, considering the optical-to-X-ray luminosity relation, a wider optical luminosity range has to be tested. As these samples already include the brightest objects, this is only possible if one can include lower optical luminosities where broad-line AGNs are not effectively selected due to an increase in the host galaxy starlight fraction. Only much deeper surveys at larger redshifts may yield the dynamical range to test the luminosity dependence for optically selected broad-line AGNs.

The possible X-ray luminosity dependence of broad-line AGN clustering detected at low redshifts (in that more X-ray luminous AGNs are more clustered than less X-ray luminous AGNs) may be difficult to reconcile with the result that, on average, low luminosity (mainly narrow-line) X-ray selected AGNs at higher redshifts are more clustered than luminous optically-selected broad-line AGNs (see Fig. 11). If the X-ray luminosity dependence is real, this may suggest that different physical processes trigger AGN activity at different cosmological times or at different luminosities.

6.6. Current Picture of AGN Clustering

Although AGN clustering measurements are currently not as constraining and the interpretation of the results is not as clear as for galaxy clustering measurements, some general findings have emerged in the last few years.

At low redshifts ($z \lesssim 0.5$), broad and narrow-line AGN cluster similarly to inactive galaxies, occupying DMH masses of $\log(M_{\text{DMH}}/[h^{-1} M_\odot]) \sim 12.0 - 13.5$. This DMH mass range includes cases where the DMH is dominated by one $\gtrsim L^*$ galaxy or a small galaxy group composed of multiple such galaxies (Zehavi et al. 2005b, 2011).

Independent of the selection method, the clustering strength of broad-line AGNs does not significantly change, while narrow-line AGNs show a significant increase in the clustering amplitude when radio-selected narrow-line AGNs are studied. Finally, more X-ray luminous broad-line AGNs may cluster more strongly than their lower luminosity counterparts. Although the various AGN samples have different luminosities, radio-loud, optically-selected narrow-line AGNs, very luminous X-ray AGNs, and red galaxies reside in somewhat similar

high DMH masses. Lower luminosity X-ray AGNs, optical narrow-line AGNs with no radio emission, and blue galaxies tend to be found in lower DMH masses.

At high redshifts ($z \gtrsim 0.7$), X-ray selected AGN samples appear to cluster more strongly than optically-selected AGNs. The reason for this remains unclear. Possibly either low-luminosity or narrow-line (X-ray absorbed) AGNs cluster more strongly than very luminous broad-line optical AGNs. Additionally, as some of the X-ray clustering studies significantly underestimate their systematic uncertainties it may turn out that these measurements are consistent with optical AGN clustering measurements. More high- z AGN clustering measurements based on larger samples are needed to gain a clearer picture.

In this paper we use AGN samples based on SDSS. In the very near future there is not another planned survey that includes photometry and a dedicated extensive spectroscopic follow-up program for AGNs over such large areas as that covered by SDSS. As both large co-moving volumes and spectroscopic redshifts are essential for precise AGN clustering measurements, major improvement in our X-ray and optically-selected low redshift AGNs are therefore not expected in the very near future. BOSS (Eisenstein et al. 2011) and BigBOSS (Schlegel et al. 2011) will detect high redshift AGNs at $z \sim 2.2$, which will improve AGN clustering measurements at higher redshifts.

In the coming years, the *ROSAT* successor *eROSITA* (Predehl et al. 2007) will perform an all-sky survey in the hard and soft X-rays, probing much fainter than RASS, which is expected to detect up to ~ 3 million AGNs. Additionally, the Large Synoptic Survey Telescope (LSST, Ivezić et al. 2008) is expected to identify ~ 2 million AGNs in optical bands. *eROSITA* and LSST have the potential to significantly improve AGN clustering measurements at low and high redshifts, though only if there are dedicated large spectroscopic follow-up programs.

7. CONCLUSIONS

This work presents AGN clustering measurements at low redshifts in three independent redshift ranges: $0.07 < z < 0.16$, $0.16 < z < 0.36$, and $0.36 < z < 0.50$. Extending the use of the cross-correlation method of Krumpe et al. (2010a), we infer the auto-correlation for both *ROSAT* All-Sky Survey (RASS) and optically-selected SDSS broad-line AGNs. As tracer sets we use SDSS main galaxies, SDSS luminous red galaxies, and very luminous red galaxies (extended LRG sample). We apply the HOD model method (Miyaji et al. 2011) directly to the measured CCFs to derive the bias parameter. We study the impact of different AGN selections on the clustering signal of broad-line AGNs, i.e., by excluding radio-detected AGNs. Furthermore, we compute the clustering strength for RASS-selected narrow-line AGNs.

We find no statistically convincing difference in the clustering of X-ray and optically-selected broad-line SDSS AGNs at low redshifts ($z < 0.5$). Different AGN selections based on either X-ray (RASS), optical (SDSS), or radio (FIRST), and combinations of these, do not significantly change the clustering signal for broad-line AGNs. This appears to be in contrast to other studies that find stronger clustering for radio-loud AGNs (e.g.,

Mandelbaum et al. 2009). However, those results are based on narrow-line, low luminosity AGNs, while our sample consists of more luminous broad-line AGNs. For the X-ray selected broad-line RASS/SDSS AGNs we find HOD bias values of $1.23^{+0.09}_{-0.08}$, $1.30^{+0.09}_{-0.08}$, and $1.02^{+0.14}_{-0.09}$ in the redshift ranges $0.07 < z < 0.16$, $0.16 < z < 0.36$, and $0.36 < z < 0.50$, respectively, while the HOD bias values for the optically selected broad-line SDSS AGNs are $0.95^{+0.17}_{-0.10}$, $1.29^{+0.05}_{-0.05}$, and $1.33^{+0.07}_{-0.08}$, respectively. The corresponding inferred typical dark matter halo masses hosting our broad-line AGNs are in the range of $\log(M_{\text{DMH}}/[h^{-1} M_{\odot}]) \sim 12.5 - 13.2$ and are consistent with those occupied by $\gtrsim L^*$ galaxies at these redshifts.

We measure the clustering of RASS selected narrow-line AGNs, which consists of a mix of NLS1s, Seyfert 1.5, 1.8, 1.9, and Seyfert 2 candidates. We do not find a significantly lower clustering amplitude of RASS narrow-line AGNs compared to broad-line AGNs, although these measurements are subject to large uncertainties. In addition, we rule out that RASS narrow-line AGNs cluster significantly more strongly than broad-line AGNs at low redshifts.

We show that the exclusion of radio-detected RASS/SDSS AGNs in $0.16 < z < 0.36$ does not change the weak X-ray luminosity dependence of the AGN clustering strength that we find in paper I (in that higher L_X AGNs cluster more strongly than lower L_X AGNs at $\sim 2\sigma$). We do not detect an optical luminosity dependence of the broad-line AGN clustering in the same redshift range, though this result is not particularly constraining due to the narrow M_i range that is covered.

We derive the bias parameter based on the best power law fit, the standard method used in literature, as well as by using HOD modeling. Important differences between the two techniques are found for some AGN samples. In particular, using a power law fit can underestimate the bias compared to HOD modeling. We show that HOD model bias parameters are more reliable and more accurately reflect the large-scale clustering strength. Larger AGN samples will be provided by future missions such

as *eROSITA*. As these samples will have lower statistical uncertainties, HOD model bias parameters should be used to avoid introducing systematic errors that could exceed the statistical errors and thus possibly lead to a misinterpretation of clustering measurements.

We would like to thank Richard Rothschild, Alex Markowitz, Slawomir Suchy, and Stephen Smith for helpful discussions. Furthermore, we thank Ryan Hickox for providing the inferred ACFs of their samples. Last but not least, we thank the referee for a very helpful report.

This work has been supported by NASA grant NNX07AT02G, CONACyT Grant Científica Básica #83564, UNAM-DGAPA Grants PAPIIT IN110209 and IN109710.

The *ROSAT* Project was supported by the Bundesministerium für Bildung und Forschung (BMBF/DLR) and the Max-Planck-Gesellschaft (MPG). Funding for the Sloan Digital Sky Survey (SDSS) has been provided by the Alfred P. Sloan Foundation, the Participating Institutions, the National Aeronautics and Space Administration, the National Science Foundation, the U.S. Department of Energy, the Japanese Monbukagakusho, and the Max Planck Society. The SDSS Web site is <http://www.sdss.org/>.

The SDSS is managed by the Astrophysical Research Consortium (ARC) for the Participating Institutions. The Participating Institutions are The University of Chicago, Fermilab, the Institute for Advanced Study, the Japan Participation Group, The Johns Hopkins University, Los Alamos National Laboratory, the Max-Planck-Institute for Astronomy (MPIA), the Max-Planck-Institute for Astrophysics (MPA), New Mexico State University, University of Pittsburgh, Princeton University, the United States Naval Observatory, and the University of Washington.

This research also made use of computing facility available from Departamento de Supercomputo, DGSCA, UNAM.

REFERENCES

- Abazajian, K., Adelman-McCarthy, J., Agüeros, M.A., et al. 2009, *ApJS*, 182, 543
- Allevato, V., Finoguenov, A., Cappelluti, N., et al. 2011, *ApJ*, 736, 99
- Anderson, S.F., Voges, W., Margon, B., et al. 2003, *AJ*, 126, 2209
- Anderson, S.F., Margon, B., Voges, W., et al. 2007, *AJ*, 133, 313
- Avni, Y., Bahcall, J.N. 1980, *ApJ*, 235, 694
- Avni, Y. & Tananbaum, H. 1986, *ApJ*, 305, 83
- Becker, R.H., White, R.L., Helfand, D.J. 1995, *ApJ*, 450, 559
- Blandford, R.D., Payne, D.G. 1982, *MNRAS*, 199, 883
- Blanton, M.R. & Roweis, S. 2007, *AJ*, 133, 734
- Blanton, M.R., Schlegel, D.J., Strauss, M.A., et al. 2005, *AJ*, 129, 2562
- Blanton, M.R., Brinkmann, J., Csabai, I., et al. 2003, *AJ*, 125, 2348
- Boyle, B.J., Shanks, T., Croom, S.M., et al. 2000, *MNRAS*, 317, 1014
- Cannon, R., Drinkwater, M., Edge, A., et al. 2006, *MNRAS*, 372, 425
- Cappelluti, N., Ajello, M., Burlon, D., et al. 2010, *ApJ*, 716, 209L
- Coil, A.L., Georgakakis, A., Newman, J.A., et al. 2009, *ApJ*, 701, 1484
- Coil, A.L., Newman, J.A., Croton, D., et al. 2008, *ApJ*, 672, 153
- Coil, A.L., Hennawi, J.F., Newman, J.A., et al. 2007, *ApJ*, 654, 115
- Colless, M., Dalton, G., Maddox, S., et al. 2001, *MNRAS*, 328, 1039
- Croom, S.M., Boyle, B.J., Shanks, T., et al. 2005, *MNRAS*, 356, 415
- Croom, S.M., Boyle, B.J., Loaring, N.S., *MNRAS*, 335, 459
- Croom, S.M., Smith, R.J., Boyle, B.J., et al. 2001, *MNRAS*, 322, 29
- da Ángela, J., Shanks, T., Croom, S.M., et al. 2008, *MNRAS*, 383, 565
- Davis, M., Faber, S.M., Newman, J., et al. 2003, *SPIE*, 4834, 161
- Davis, M., Peebles, P.J.E. 1983, *ApJ*, 267, 465
- Dodelson, S., *Modern cosmology*, Amsterdam (Netherlands): Academic Press. ISBN 0-12-219141-2
- Eisenstein, D.J., Weinberg, D.H., Agol, E., et al. 2011, *arXiv:1101.1529*
- Eisenstein, D.J., Annis, J., Gunn, J.E., et al. 2001, *AJ*, 122, 2267
- Eisenstein, D.J. & Hu 1998, *ApJ*, 496, 605
- Gilli, R., Zamorani, G., Miyaji, T., et al. 2009, *A&A*, 494, 33
- Gilli, R., Daddi, E., Zamorani, G., et al. 2005, *A&A*, 430, 811
- Grazian, A., Negrello, M., Moscardini, L., et al. 2004, *AJ*, 127, 592
- Green, P.J., Scharrel, N., Anderson, S.F. et al. 1995, *ApJ*, 450, 51
- Halpern, J.P., Turner, T.J., George, I.M. 1999, *MNRAS*, 307, L47
- Hamilton, A.J.S. 2001, *MNRAS*, 322, 419
- Hamilton, A.J.S., Tegmark, M. 2004, *MNRAS*, 349, 115
- Hickox, R.C., Jones, C., Forman, W.R., et al. 2009, *ApJ*, 696, 891

- Ivezic, Z., Tyson, J.A., Acosta, E., et al. 2008, arXiv:0805.2366
- Kauffmann, G., Heckman, T.M., Tremonti, C., et al. 2003, MNRAS, 346, 1055
- Kellermann, K.I., Sramek, R., Schmidt, M., Shaffer, D.B., & Green, R. 1989, AJ, 98, 1195
- Kochanek, C.S., Eisenstein, D., Caldwell, N., et al. 2004, AAS, Meeting 205, #94.02, Vol.36, 1495
- Krumpe, M., Lamer, G., Markowitz, A., Corral, A. 2010b, ApJ, 725, 2444
- Krumpe, M., Miyaji, T., & Coil, A.L. 2010a, ApJ, 713, 558 (paper I)
- Krumpe, M., Lamer, G., Schwobe, A.D., et al. 2007, A&A, 466, 41
- Landy, S.D., Szalay, A.S. 1993, ApJ, 412, 64
- Larson, D., Dunkley, J., Hinshaw, G., et al. 2011, ApJS, 192, 16
- Le Fèvre, O., Vettolani, G., Garilli, B., et al. 2005, A&A, 439, 845
- Li, C., Kauffmann, G., Wang, L., et al. 2006, MNRAS, 373, 457
- Limber, D. N. 1954, ApJ, 119, 655
- Madgwick, D.S., Hawkins, E., Lahav, O., et al. 2003, MNRAS, 344, 847
- Magliocchetti, M., Maddox, S.J., Hawkins, E., et al. 2004, MNRAS, 350, 1485
- Mandelbaum, R., Li, C., Kauffmann, G., White, S.D.M., et al. 2009, MNRAS, 393, 377
- Meneux, B., Le Fèvre, O., Guzzo, L., et al. 2006, A&A, 387, 395
- Meneux, B., Guzzo, L., de la Torre, S., et al. 2009, A&A, 505, 463
- Miyaji, T., Krumpe, M., Coil, A.L., Aceves, H. 2011, ApJ, 726, 83 (paper II)
- Mountrichas, G., Sawangwit, U., Shanks, T., et al. 2009, MNRAS, 394, 2050
- Mullis, C.R., Henry, J.P., Gioia, I.M., et al. 2004, ApJ, 617, 192
- Navarro, J.F., Frenk, C.S., White, S.D.M., 1997, ApJ, 490, 493
- Norberg, P., Baugh, C.M., Hawkins, E., et al. 2002, MNRAS, 332, 827
- Padmanabhan, N., Schlegel, D.J., Finkbeiner, D.P., et al. 2008, ApJ, 674, 1217
- Peebles, P.J.E., The Large-Scale Structure of the Universe, Princeton, N.J., Princeton Univ. Press
- Porciani, C., Magliocchetti, M., Norberg, P. 2004, MNRAS, 355, 1010
- Porciani, C., Norberg, P., 2001, MNRAS, 371, 1824
- Predehl, P., Andritschke, R., Bornemann, W., et al. 2007, SPIE, 6686, 36
- Richards, G.T., Fan, X., Newberg, H.J., et al. 2002, AJ, 123, 2945
- Ross, N.P., Shen, Y., Strauss, M.A., et al. 2009, ApJ, 697, 1634
- Savitzky, A., Golay, M.J.E. 1964, Anal. Chem., 36, 1627
- Schlegel, D.J., Abdalla, F., Abraham, T., et al. 2011, arXiv:1106.1706
- Schmidt, M. & Green, R.F. 1983, ApJ, 269, 352
- Schneider, D.P., Richards, G.T., Hall, P.B., et al. 2010, AJ, 139, 2360
- Schneider, D.P., Hall, P.B., Richards, G.T., et al. 2007, AJ, 134, 102
- Serber, W., Bahcall, N., Menard, B., & Richards, G. 2006, ApJ, 643, 68
- Shen, Y., Strauss, M.A., Ross, N.P., et al. 2009, ApJ, 697, 1656
- Sheth, R.K., Mo, H.J., Tormen, G. 2001, MNRAS, 323, 1
- Spergel, D.N., Verde, L., Peiris, H.V., et al. 2003, ApJS, 148, 175
- Steffen, A.T., Strateva, I., Brandt, W.N. et al. 2006, ApJ, 131, 2826
- Strand, N.E., Brunner, R.J., Myers, A.D. 2008, ApJ, 688, 180
- Strauss, M.A., Weinberg, D.H., Lupton, R.H., et al. 2002, AJ, 124, 1810
- Tinker, J.L., Weinberg, D.H., Zheng, Z., & Zehavi, I. 2005, ApJ, 631, 41
- Veilleux, S. & Osterbrock, D.E. 1987, ApJS, 63, 295
- Voges, W., Aschenbach, B., Boller, T., et al. 1999, A&A, 349, 389
- Wake, D.A., Miller, C.J., Di Matteo, T., et al. 2004, ApJ, 610, 85
- White, R.L., Becker, R.H., Helfand, D.J., Gregg, M.D., 1997, ApJ, 475, 479
- Wilkes, B.J., Tananbaum, H., Worrall, D.M., et al. 1994, ApJS, 92, 53
- Yang, Y., Mushotzky, R.F., Barger, A.J., Cowie, L.L. 2006, 645,68
- Zehavi, I., Zheng, Z., Weinberg, D.H., et al. 2010, ApJ, 736, 59
- Zehavi, I., Eisenstein, D.J., Nichol, R.C., et al. 2005, ApJ, 621, 22
- Zehavi, I., Zheng, Z., Weinberg, D.H., et al. 2005, ApJ, 630, 1
- Zheng, Z., Zehavi, I., Eisenstein, D. J., Weinberg, D. H., & Jing, Y. P. 2009, ApJ, 707, 554
- Zheng, Z., Coil, A.L., & Zehavi, I. 2007, ApJ, 667, 760